

Evaluating the QSO contribution to the 21-cm signal from the Cosmic Dawn

Hannah E. Ross,^{1,2,3}  Keri L. Dixon,^{4,2} Raghunath Ghara,³ Ilian T. Iliev,² and Garrelt Mellema³

¹ Computational Cosmology Center, Computational Research Division, Lawrence Berkeley National Lab, Berkeley, CA 94720

² Astronomy Centre, Department of Physics & Astronomy, Pevensey III Building, University of Sussex, Falmer, Brighton, BN1 9QH, United Kingdom

³ Department of Astronomy & Oskar Klein Centre, AlbaNova, Stockholm University, SE-106 91 Stockholm, Sweden

⁴ New York University Abu Dhabi, PO Box 129188, Saadiyat Island, Abu Dhabi, UAE

Accepted ?; Received ??; in original form ???

ABSTRACT

The upcoming radio interferometer Square Kilometre Array (SKA) is expected to directly detect the redshifted 21-cm signal from the neutral hydrogen present during the Cosmic Dawn. Temperature fluctuations from X-ray heating of the neutral intergalactic medium can dominate the fluctuations in the 21-cm signal from this time. This heating depends on the abundance, clustering, and properties of the X-ray sources present, which remain highly uncertain. We present a suite of three new large-volume, 349 Mpc a side, fully numerical radiative transfer simulations including QSO-like sources, extending the work previously presented in Ross et al. (2017). The results show that our QSOs have a modest contribution to the heating budget, yet significantly impact the 21-cm signal. Initially, the power spectrum is boosted on large scales by heating from the biased QSO-like sources, before decreasing on all scales. Fluctuations from images of the 21-cm signal with resolutions corresponding to SKA1-Low at the appropriate redshifts are well above the expected noise for deep integrations, indicating that imaging could be feasible for all the X-ray source models considered. The most notable contribution of the QSOs is a dramatic increase in non-Gaussianity of the signal, as measured by the skewness and kurtosis of the 21-cm probability distribution functions. However, in the case of late Lyman- α saturation, this non-Gaussianity could be dramatically decreased particularly when heating occurs earlier. We conclude that increased non-Gaussianity is a promising signature of rare X-ray sources at this time, provided that Lyman- α saturation occurs before heating dominates the 21-cm signal.

Key words: cosmology: theory — radiative transfer — reionization — intergalactic medium — large-scale structure of universe — galaxies: formation

1 INTRODUCTION

The Epoch of Reionization, hereafter EoR, is the cosmological era during which the first luminous sources reionized the Universe. Observations of the high-redshift Lyman- α forest (e.g. McGreer et al. 2015; Davies et al. 2018; Bosman et al. 2018), an observed decrease in Lyman- α emitting galaxies at high redshifts (e.g. Pentericci et al. 2014; Tilvi et al. 2014; De Barros et al. 2017; Mason et al. 2018), and temperature measurements of the high-redshift intergalactic medium (IGM; e.g. Raskutti et al. 2012; Bolton et al. 2012) indicate reionization ended sometime before $z \approx 5.7$. The start of substantial reionization (i.e. more than 10 per cent of the hydrogen mass) is constrained to be redshift 10 by the measured Thomson optical depth for CMB scattering (e.g. Planck Collabora-

tion 2016). Other than these constraints on the timing of the EoR, the astrophysics of this era remains extremely uncertain.

The most powerful observational probe of this epoch is the redshifted 21-cm signal originating from the hyperfine spin-flip transition of hydrogen. Three experiments are currently attempting to measure the 21-cm signal from the EoR using low-frequency radio interferometry: LOFAR¹, MWA² and PAPER³. The LOFAR collaboration has recently set an upper limit to the 21-cm power spectrum from the Epoch of reionization (Patil et al. 2017) and similar constraints were previously published based on data from GMRT⁴ (Paciga et al. 2011, 2013). PAPER also placed constraints

¹ <http://www.lofar.org/>

² <http://www.mwatelescope.org/>

³ <http://eor.berkeley.edu/>

⁴ <http://gmrt.ncra.tifr.res.in/>

* email: HRoss@lbl.gov

on the 21-cm power spectrum (Ali et al. 2015), but have since retracted these claims (Ali et al. 2018). The future interferometers HERA⁵ and SKA⁶ are expected to be able to detect and possibly image the EoR.

The beginning of the EoR, when the first luminous sources start to appear but reionization is not yet fully under way, is referred to as the Cosmic Dawn (CD). During this period, the gas temperature fluctuations in the neutral IGM are likely to be the dominant contributor to 21-cm fluctuations (see Section 3 for more details). The neutral IGM can only be heated by X-ray photons as they have long mean free paths and are thus able to travel far from their origin, penetrating deep into the neutral hydrogen regions. In contrast, the UV photons produced by stars have short mean free paths and only heat and ionize very locally. Therefore, the 21-cm signal from these early stages of reionization is expected to be sensitive to the spectra, abundance, and clustering of any X-ray sources present at this time. The Experiment to Detect the Global EoR Signature, EDGES⁷, has recently claimed to have detected an extremely strong absorption signal from the CD (Bowman et al. 2018). If this result is confirmed then additional physics is required to explain the measured signal. The observational difficulties of this experiment and concerns over the foreground modeling (Hill & Baxter 2018) lead us to conclude that further validation from another independent observation is required in order to verify the result.

The nature of X-ray sources present in the CD sources remains extremely uncertain. Simulations have suggested that the first generation of stars (Population III stars, referred to as Pop III stars hereafter) could have formed binary systems as early as redshift 30 (Glover & Brand 2003). High-mass X-ray binaries, HMXBs, have therefore been suggested as significant contributors to the X-ray emissions (e.g. Xu et al. 2014; Jeon et al. 2014; Chen et al. 2015). QSOs are also a likely candidate for early X-ray heating. Chardin et al. (2015) argued that the observation of a large scatter in the Lyman- α opacity in Becker et al. (2015) suggests patchy hydrogen reionization, implying the presence of rare, bright sources. The presence of high-redshift QSOs is also consistent with the gentle slope at the bright-end of the high-redshift UV galaxy luminosity at $z \sim 7$ (Bowler et al. 2012; Bowler 2014; Bowler et al. 2015) and the X-ray spectra associated with these galaxies (Stark et al. 2015a,b, 2017; Mainali et al. 2017). An observation of high-redshift, low-luminosity QSOs in Giallongo et al. (2015) has suggested that the low-mass end of the QSO X-ray luminosity functions (QXLF) may be steeper than previously thought. Grissom et al. (2014); Giallongo et al. (2015); Chardin et al. (2015); Khaire et al. (2016) and Mitra et al. (2018) argue that QSOs may even be numerous enough to contribute significantly to reionization itself. Contrarily, Onoue et al. (e.g. 2017); Oñorbe et al. (e.g. 2017); Qin et al. (e.g. 2017); Hassan et al. (e.g. 2018); Akiyama et al. (e.g. 2018) and Parsa et al. (2018) argue that QSOs are unlikely to contribute significantly to reionization.

Multiple theoretical studies have previously investigated the impact of X-ray heating during the CD. Early work on this topic was analytical (e.g. Glover & Brand 2003; Furlanetto et al. 2004) and considered a simple X-ray background. However, most recent works have focused on semi-numerical (see e.g. Santos et al. 2010; Mesinger et al. 2013; Fialkov et al. 2014; Kneivt et al. 2014; Ghara et al. 2016, 2017; Greig & Mesinger 2018; Das et al. 2017; Douna

et al. 2018) and numerical (eg. Xu et al. 2014; Ahn et al. 2015a; Ross et al. 2017) modeling. These works consider the dominant contributors of X-rays in the CD to be HMXBs and, therefore, trace the stellar population. There is disagreement on the contribution of HMXBs. For example, Kneivt et al. (2014) find that HMXBs do not contribute significantly to the CD; whereas, Greig & Mesinger (2018) predict that the heating during the CD will be detectable by SKA. These differences stem from the lack of understanding of high redshift HMXBs, and of high redshift sources in general.

QSO source models have also been investigated in previous works both using semi-numerical (e.g. Yajima & Li 2014; Datta et al. 2016; Qin et al. 2017; Hassan et al. 2018) and numerical (e.g. Baek et al. 2010; Kakiichi et al. 2017; Semelin et al. 2017; Eide et al. 2018) methods. The large scale fully numerical simulations run by Kakiichi et al. (2017) and semi-numerical simulations run by Hassan et al. (2018) and Qin et al. (2017) focus on the impact of QSOs during the EoR rather than the CD. Datta et al. (2016) investigate an individual QSO and assume the luminosity to be the same as a the high redshift QSO observation from Mortlock et al. (2011). They focus primarily on the detectability of an individual QSO source rather than their contribution to reionization and heating process.

The luminosities of the QSOs are often calculated by assuming black hole masses are proportional the mass of stars in the galaxy and are accreting at the Eddington limit. For example, Yajima & Li (2014) have considered individual sources in a comparable way to Datta et al. (2016), but assuming the luminosity of QSOs to be proportional to the mass of the halo. While there has been an observed correlation between the mass of the bulge of galaxies and the masses of their central black holes (e.g. Häring & Rix 2004; Läscher et al. 2016), it has been known for a long time that this relationship does not extend to the luminosity of the QSO (e.g. Woo & Urry 2002). Baek et al. (2010) and Eide et al. (2018) have used this assumption that $L \propto M_{\text{halo}}$ in their detailed fully numerical simulations of QSOs during the CD including the radiative transfer ionizing UV photons, X-rays, and Lyman- α photons, albeit with a smaller boxsize ($\sim 100 \text{ Mpc } h^{-1}$).

In this paper, we extend our suite of numerical simulations of the inhomogeneous heating during the CD previously presented in Ross et al. (2017), hereafter referred to as Paper I, with the addition of different X-ray emitter models. Using the same cosmic density fields and halo lists, we compare the morphology and evolution of the 21-cm signal for these different cases. We also include a Lyman- α background in order to comment on the possible impact of late Lyman- α saturation. Our simulations are sufficiently large to capture the large-scale patchiness of reionization and to make statistically meaningful predictions for future 21-cm observations.

The outline of the paper is as follows. In Section 2, we present our N -body and radiative transfer simulations and describe our different X-ray source models. In Section 3, we summarize the extraction of the 21-cm signatures from our simulations. In Section 4, we describe our semi-numerical radiative transfer of Lyman- α photons. Section 5 contains our results, primarily comparisons between the different source models. We then conclude in Section 6. The cosmological parameters we use throughout this work are $(\Omega_{\Lambda}, \Omega_{\text{M}}, \Omega_{\text{b}}, n, \sigma_8, h) = (0.73, 0.27, 0.044, 0.96, 0.8, 0.7)$; where the notation has the usual meaning and $h = H_0/(100 \text{ km s}^{-1} \text{ Mpc}^{-1})$. These values are consistent with the latest results from WMAP (Komatsu et al. 2011) and Planck combined with all other available constraints (Planck Collaboration et al. 2015; Planck Collaboration 2016).

⁵ <http://reionization.org/>

⁶ <https://www.skatelescope.org/>

⁷ <http://loco.lab.asu.edu/edges/>

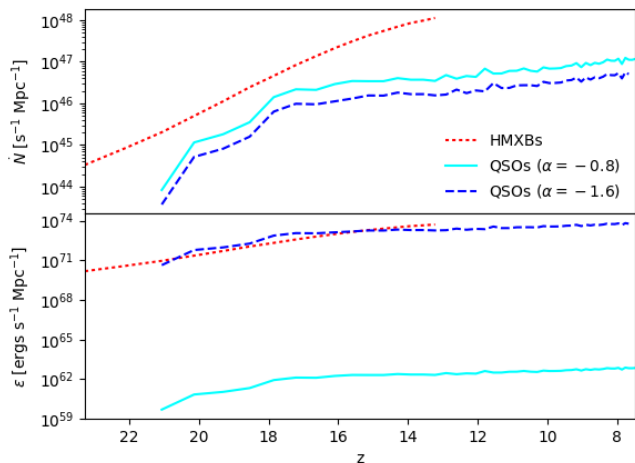


Figure 1. The ionizing photon rate (top panel) and emissivity (bottom panel) of each source type. f_X is not fundamental to our method so we do not show it here.

2 METHODOLOGY

2.1 THE SIMULATIONS

The density fields and halo catalogues were obtained from a high-resolution, N -body simulation (presented in Dixon et al. (2016), and also used in Paper I). This simulation was run using the CUBEP³M Code (Harnois-Déraps et al. 2013) and followed 4000³ particles in a 349 comoving Mpc per side volume to enable reliable halo identification down to $10^9 M_\odot$.

The radiative transfer simulations were run using the latest version of the photon conserving, short characteristics ray-tracing method C²-RAY code (Mellema et al. 2006) over a grid-size of 250³ with a timestep of 11.52 Myrs. The original version was updated in order to accommodate higher energy photons and track the temperature of the IGM (Friedrich et al. 2012). These modifications included the inclusion of multi-frequency heating, the inclusion of all three species of helium, and a full on-the-spot approximation in order to model secondary ionizations. To be able to correctly handle unresolved ionized regions, we developed a new, multiphase, approach, described below in Section 3.1 and Appendix A.

A total of five simulations are presented: a simulation with only stellar sources (S1), another two with both stellar sources and QSO sources with power laws of different spectral indices (S2, S3), a simulation with both stellar and HMXB sources (S4), and a simulation with stellar sources, HMXBs, and the harder QSO sources (S5). Information about the spectral indices of the X-ray sources are given in Table 1, and the source details are outlined in Section 2.2. S1 and S4 have previously been presented in Paper I and S5 in Ross et al. (2018). S2 and S3 were run with the new multiphase version of the code.

2.2 SOURCES

We consider three types of ionization sources: stellar sources, HMXBs, and QSOs. The total number of ionizing photons, \dot{N} , and emissivity, ϵ , of each type of source are shown in Fig. 1. We plot \dot{N} and ϵ rather than f_X as the calculation of the later requires assumptions about N_i and f_{esc} .

2.2.1 Stellar sources

Stellar sources form inside dark matter haloes. High-Mass Atomically Cooling Haloes, HMACHs, are haloes with masses greater than $10^9 M_\odot$ and are resolved by the N -body simulation, from which they were extracted using the spherical over-density algorithm. HMACHs have sufficiently deep gravitational wells to accrete surrounding IGM gas, even when the gas has been photoheated. Furthermore, their gas virial temperatures are above 10^4 K, allowing the gas to efficiently cool through hydrogen and helium atomic line radiation. Therefore, these haloes are able to keep accreting fresh gas and forming stars regardless of their local ionization. We therefore assume these sources to be un-suppressible, i.e. continually forming stars end emitting photons into the IGM.

Haloes of lower mass are not able to accrete IGM gas with temperatures around 10^4 K; however, haloes above $10^8 M_\odot$ are capable of accreting cold IGM gas, as it can cool to sufficiently low temperatures through atomic lines. These Low Mass Atomically Cooling Haloes, LMACHs, are able to gravitationally bind neutral, but not ionized gas. In reality there is no sharp cut-off between HMACHs and LMACHs, rather a gradual decrease in the amount of cold gas which can be retained with declining halo mass (Efstathiou 1992; Navarro & Steinmetz 1997; Dijkstra et al. 2004; Hasegawa & Semelin 2013). However, for simplicity we assumed that LMACHs residing in cells that are more than 10 percent ionized are assumed to not form stars, i.e. they are suppressed (Iliev et al. 2007; Dixon et al. 2016). This is in rough agreement with recent results from detailed fully-coupled radiative hydrodynamics simulations, though the suppression mass and level of suppression depend on the strength of supernova feedback (Wise & Abel 2008; Ocvirk et al. 2016; Dawoodbhoy et al. 2018; Ocvirk et al. 2018).

LMACHs are not resolved by the N -body simulation and are added using a sub-grid model (Ahn et al. 2015b) that is calibrated against higher mass resolution simulations of smaller volumes. We do not take into account the redshift dependence of the cut-off mass at which haloes are no longer able to accrete ionized gas; however, this effect is minor (Shapiro et al. 1994).

Stellar sources are assigned a blackbody spectrum with an effective temperature of $T_{\text{eff}} = 5 \times 10^4$ K, which is consistent with observations of O and B stellar spectra. The luminosity of the sources is proportional to the mass of their host haloes:

$$\dot{N}_\gamma = g_\gamma \frac{M\Omega_b}{m_p(10 \text{ Myr})\Omega_{t_0}}, \quad (1)$$

where g_γ is the photon production efficiency factor. Here, g_γ is given by:

$$g_\gamma = f_* f_{\text{esc}} N_i \frac{10 \text{ Myr}}{\Delta t}, \quad (2)$$

where f_* is the star formation efficiency, f_{esc} is the escape fraction, N_i is the ionizing photon efficiency per stellar baryon, and Δt is the lifetime of the source. LMACHs are given a higher value of g_γ (7.1) than HMACHs (1.7), which reflects the likely presence of larger, more efficient Pop III stars (Stacy et al. 2016) and/or higher escape fractions (e.g. Xu et al. 2016; Chisholm et al. 2018). These stellar spectra produce minimal X-rays, so do not contribute significantly to the heating of the neutral IGM. For more details on the implementation of these sources, see LB2 of Dixon et al. (2016).

2.2.2 HMXBs

The HMXB sources are assumed to reside in dark matter haloes and to have power-law spectra:

$$L_h(\nu) \propto \nu^{-\alpha_x^h}, \quad (3)$$

where $\alpha_x^h = 1.5$. The energy range extends from 272.08 eV to 100 times the second ionization of helium (5441.60 eV). The low-frequency cut-off corresponds to the obscuration suggested to be present by observational works (e.g. Lutovinov et al. 2005) and is consistent with the optical depth from high-redshift, gamma-ray bursts (Totani et al. 2006; Greiner et al. 2009). As with the stellar sources, the luminosity is related to the mass of the host halo via equation (1), but with a lower value of g_γ (0.086) for all haloes. g_γ is given by equation (2) with $f_{\text{esc}}=1$ and N_x (the number of X-ray photons produced per stellar baryon) in place of N_i . The X-ray luminosities are roughly consistent with measurements of X-ray binaries in local, star-bursting galaxies (Mineo et al. 2012). For more details on the implementation of these sources, see Paper I.

2.2.3 QSO sources

Due to the lack of suitable high redshift observations, we must make some assumptions about the luminosity and spectra of the QSOs present during the CD. We assume that our QSO-like sources only produce X-rays, which physically means that stellar sources dominate the lower frequency photon budget.⁸ The X-ray emissivity from QSOs is quantified using the QXLF. Here, we follow Ueda et al. (2014, see section 6.2 for the functional form and table 4 for the parameter values), though modified to reflect the uncertainty in the higher redshift behaviour. In particular, we alter the high-redshift (in this case, $z > 3$) density evolution parameter (known as $p3 = -6.2$ in Ueda et al. 2014) to a smaller -2, which is more in line with Giallongo et al. (2015) or generally including more QSOs at high redshift. Furthermore, one aim of this paper is to investigate the maximal impact of these type of sources; though, we concede that such a shallow QSO density evolution is unlikely at the highest redshifts. This QXLF takes the form of a double power law with luminosity-dependent density evolution and is taken over an X-ray luminosity (L_x) range of $10^{42} - 10^{47}$ ergs s^{-1} .

The number density of QSOs in our simulation volume, n_q , is calculated by integrating the QXLF, $\Phi(L, z)$, for each redshift

$$n_q(z) = \int_{L_{\text{min}}}^{L_{\text{max}}} \Phi(L, z) dL, \quad (4)$$

where $\Phi \propto (1+z)^{-2}$ is the QXLF. At high redshift, the number density of haloes capable of hosting quasars (i.e., the HMACHs number density) is insufficient to replicate the QXLF (see below for host halo details).

The QSO spectrum is assumed to be:

$$L_q(\nu) \propto \nu^{-\alpha_x^q}, \quad (5)$$

where $\alpha_x^q = 0.8$ (Ueda et al. 2014) or 1.6 (Brightman et al. 2013) for our two QSO models. More generally, we chose a hard and soft

model, where the exact spectral indices are unimportant, for comparison sake. The luminosity of each QSO at 2 keV is then assigned by randomly sampling the QXLF. Given this luminosity and spectral index, \dot{N}_γ is calculated for the same frequency (energy) range as the HMXBs.

The luminosities of observed QSOs do not correlate with the mass of their host galaxy or that of the central black hole, but rather depend on the physics of the accretion disk (e.g. Woo & Urry 2002; Middei et al. 2017). Consequently, in our simulations, we place the active QSOs in random HMACH haloes.⁹ Initially, HMACHs are too rare to host sufficient numbers of QSOs to reproduce the (admittedly optimistic) luminosity function. At these early times, we assign a single QSO to each existing HMACH halo. Furthermore, in our simulations, we assume a QSO lifetime of 34.56 Myr, which is consistent with current estimates (e.g. Borisova et al. 2016; Khrykin et al. 2017). It has been long known that the luminosity of QSOs varies with time over all frequencies, including the X-ray range of the spectrum (e.g. Halpern 1984; Pan et al. 1990; Jin et al. 2017), and we mimic this behaviour by assigning a new L_q every 11.52 Myr, with a value that is within an order of magnitude of the previous L_q .

3 THE 21-CM SIGNAL

We are primarily interested in the 21-cm signal observable, the differential brightness temperature with respect to the CMB, δT_b , given by:

$$\delta T_b = \left(1 - \frac{T_{\text{CMB}}}{T_S}\right) \frac{3\lambda_0^3 A_{10} T_* n_{\text{HI}}(z)}{32\pi H(z)(1+z)}, \quad (6)$$

where $\lambda_0 = 21.1$ cm is the line rest-frame wavelength, $A_{10} = 2.85 \times 10^{-15} \text{ s}^{-1}$ is the Einstein A -coefficient for spontaneous emission from the triplet to singlet state, n_{HI} is the density of neutral hydrogen, and T_S is the spin temperature.

The T_S reflects the relative number of atoms in the singlet and triplet state of the 21-cm line, given by (Field 1958):

$$T_S = \frac{T_{\text{CMB}} + y_\alpha T_\alpha + y_c T_K}{1 + y_\alpha + y_c}, \quad (7)$$

where T_α is the radiation colour temperature, T_K is the kinetic temperature of the gas, and y_α and y_c are the coupling coefficients corresponding to the Lyman- α decoupling (the Wouthuysen-Field effect) and collisional decoupling, respectively. In the absence of decoupling mechanisms (collisions between atoms or Lyman- α pumping), the 21-cm line is in equilibrium with the CMB, and thus $T_S = T_{\text{CMB}}$.

The y_α is calculated using:

$$y_\alpha = \frac{T_* P_{10}}{T_K A_{10}}, \quad (8)$$

where P_{10} is the radiative de-excitation rate due to Lyman- α photons ($\sim 10^9 J_\alpha$, where J_α is the Lyman- α flux), and $T_* = 0.068$ K is the temperature corresponding to the energy difference between two the states.

In the case of early Lyman- α saturation, y_α becomes large everywhere, and $T_S \approx T_K$, as we assumed in Paper I. However, in

⁸ Note that by considering only the X-ray photons, we are neglecting the UV contribution from QSOs. Within our model and at these high redshifts, we do not expect a large impact on our results, but some comparisons to other studies may be complicated by this fact.

⁹ In rare cases, an HMACH will disappear for some reason, such as stripping or merging. In this circumstance, we reassign a brand new QSO elsewhere that is sampled from the current redshift's QXLF.

Table 1. Table showing the spectral index of our X-ray sources in different runs. All simulations include stellar sources with a blackbody spectrum corresponding to a temperature of 5×10^4 K.

Spectral index	S1	S2	S3	S4	S5
α_x^h	–	–	–	1.5	1.5
α_x^q	–	0.8	1.6	–	0.8

the case of late Lyman- α saturation, we must include the additional fluctuations as a post-processing step (see Section 4).

It is not necessary to include collisional coupling at the redshifts we consider. The Universe has expanded enough that the density of the IGM is insufficient to produce non-negligible collisions between hydrogen atoms. In addition, we do not resolve the dark matter filaments with sufficient densities for collisional coupling to become efficient on the RT grid.

3.1 T_K AND RESOLUTION EFFECTS

It is not computationally feasible to resolve the small scales (of the order of kpc) corresponding to the width of ionization fronts or (more importantly in the CD) small H II regions while including the larger scales. In the original version of C²-RAY, cells containing ionization fronts or small H II regions are partially ionized and contain an averaged temperature and ionized fraction. While these average values themselves are correct, using them to calculate δT_b can yield an incorrect result. Consider a cell that contains a small, hot, ionized bubble and a cold, neutral region. When calculating δT_b , the ionized region should not contribute, but in this case the high temperature of the ionized region will dramatically increase the average value the T_K of hydrogen in the cell, and hence the δT_b , will be overestimated. This problem is particularly pronounced during the CD when many small ionized regions enclosed in single cells are present due to our mass resolution being much higher than our RT resolution.

As described in detail in Paper I, this problem was resolved via post-processing of the simulation using a second simulation without X-ray sources. While sufficient at the redshifts and for the X-ray source model of the simulations in Paper I, this method breaks down at $z \sim 11$, as a significant number of stellar sources are able raise the temperature high enough for collisional cooling to become efficient. More efficient cooling in the X-ray simulation compared to the stellar simulation results in the temperature being underestimated (see Appendix B3 for more details on this).

For the current work, we have developed a new version of C²-RAY that includes a multiphase, subgrid modeling of the IGM to track the temperatures of the ionized and neutral IGM separately. Not only is this method much more robust and accurate, but it is also significantly more computationally efficient as only one simulation is required. Appendix A provides a more detailed description of our new algorithm and test boxes, and Appendix B presents results of two tests that demonstrate the differences between the old and new algorithm.

4 LYMAN- α COUPLING

The amount of emitted soft (i.e. non-ionizing) UV photons that subsequently redshift into the Lyman- α resonance is very uncer-

tain. Here we consider the two extremes: very early and very late Lyman- α saturation scenarios in order to demonstrate the full range of these uncertain source parameters. We leave a more detailed analysis of the impact of Lyman- α photons for future work.

Early mini-haloes (haloes with masses below $\sim 10^8 M_\odot$ that host the First Stars) may contribute significantly to the Lyman- α background, which could result in Lyman- α saturation occurring quite early. In the most extreme scenario, a strong Lyman- α background may have already been built up by mini-haloes before our simulation has begun ($z \sim 23$), as was assumed in Paper I.

At the other end of the possible range, mini-haloes might contribute very little Lyman- α radiation, so the Lyman- α background is only built up by the HMACHs and LMACHs. In this scenario, we must consider the inhomogeneous background they produce.

Fully numerical radiative transfer simulations of Lyman- α are computationally expensive and, in this case, largely unnecessary. On large scales, a $1/r^2$ profile (where r is the radial distance from the source) has been shown to be consistent with detailed radiative transfer in Semelin et al. (2007); Vonlanthen et al. (2011) and Higgin & Meiksin (2012). In addition, the Lyman- α photons from a point source have been shown to produce a nearly spherical profile even in the presence of density fluctuations (Vonlanthen et al. 2011).

Here we employ the method used previously in Ghara et al. (2016), assuming this $1/r^2$ spherical profile with a few improvements. In order to calculate the Lyman- α flux, J_α , from the simulations, we use SEDs generated by the stellar population synthesis code PEGASE2 (Fioc & Rocca-Volmerange 1999). Galaxies are initially metal-poor ($10^{-3} Z_\odot$, where Z_\odot is solar metallicity) and are assumed to have a Salpeter initial mass function (with stars with masses between 1 and 100 M_\odot). Our method was updated compared to previous versions so that the flux of the Lyman- α photons depend on the mass of the source when they were emitted (i.e. to use the retarded luminosity). This allows us to take into account the variations in luminosity of the sources due to the changing mass of dark matter haloes, the suppression of LMACHs and the movement of the haloes.

For these calculations, we assume the escape fraction of the ionizing photons to be 10 per cent, and the escape fraction of non-ionizing UV photons to be 100 per cent. Some observations have shown high redshift galaxies to be dustier than expected (e.g. Vieira et al. 2013; Watson et al. 2015; Laporte et al. 2017; Chiaki & Wise 2019; Tamura et al. 2019). It is important to note that it is possible that early dust enrichment could reduce the fraction of Lyman- α photons that escape.

5 RESULTS

5.1 Global Histories

In Fig. 2 we show the global histories of the ionization, neutral gas temperature and Lyman- α coupling coefficient of our simulations. The top panel shows the volume averaged ionized fraction, \bar{x}_H . All sources follow a similar reionization history as, despite producing photons capable of ionizing more than one atom, X-ray sources yield far fewer photons overall than their stellar companions.

Although X-ray photons are rare, they lead to significant photo-heating as we can see from the middle panel of Fig. 2 which displays the volume averaged temperature, \bar{T}_K . X-ray heating progresses more rapidly in the cases including HMXBs than those with only QSOs.

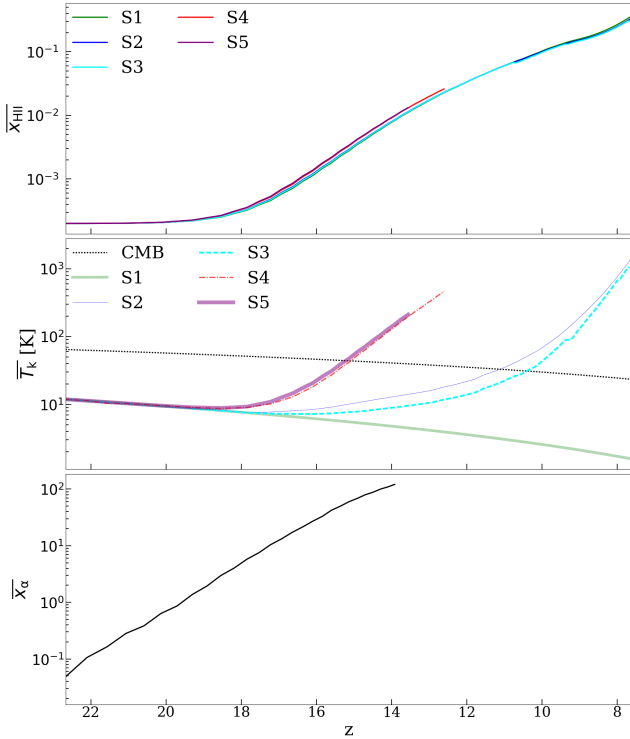


Figure 2. The global histories of the volume-averaged ionized fraction ($\overline{x_{\text{H}}}$; top), the volume-averaged kinetic temperature of the neutral gas ($\overline{T_{\text{K}}}$; middle) and the volume-average value of the Lyman- α coupling coefficient ($\overline{x_{\alpha}}$; bottom). Note that some curves have significant overlap, particularly for the reionization history.

Finally, in the bottom panel the volume averaged value of the Lyman- α coupling coefficient, $\overline{x_{\alpha}}$, is shown. $\overline{x_{\alpha}}$ follows the same evolution in all the simulations as the sources Lyman- α are near identical. After $z \approx 14$ the Lyman- α becomes saturated.

Our global heating histories are very different to those found in e.g. Semelin et al. (2017). In their models significant ionization, heating and Lyman- α coupling occur considerably later than here. They find that typically this occurs below $z \sim 10$, with peak around $z \sim 8$. The main reason for these differences is that those simulations only include fairly massive sources, $M > 10^{10} M_{\odot}$, which are very rare during reionization and only appear in significant numbers late.

5.2 Evolution of the signal

In Fig. 3, we show the δT_{b} lightcones, slices from the position-redshift image cube, for each of the five simulations. We show only late Lyman- α saturation, meaning that all models start with $\delta T_{\text{b}} = 0$. When compared to the results in Paper I, we see that the inclusion of the Lyman- α coupling effect in this case yields a weaker absorption signal, since heating is already underway before Lyman- α saturation ($y_{\alpha} \gg 1$) is reached. The inhomogeneous Lyman- α background also softens the features present before Lyman- α saturation ($z \approx 17$). Unless stated otherwise, the late Lyman- α saturation case is the default.

After the Lyman- α background saturates, δT_{b} in simulation S1 remains in absorption for the rest of the simulation due to the lack of photons with long enough mean free paths to penetrate

Table 2. Table showing the expected noise on SKA1-Low from (Koopmans et al. 2015) for a maximum baseline of 1.2 km and an integration time of 1000 h.

z	8.95	15.98	25.25
θ [arcmin]	6.0	10.3	15.8
δT_{b} [mK]	4	5	20

and heat the neutral IGM. Hence, the transition from absorption to emission never occurs in this case. At later times, ionized patches indicating the beginning of significant ionization can be seen as holes ($\delta T_{\text{b}} \approx 0$) in the HI distribution.

In S2 and S3, the signal remains largely in absorption for longer than in S4 and S5, due to the total X-ray photon budget from the QSO sources being much lower than that of the HMXBs. However, at $z \approx 16.5$, patches of higher δT_{b} start to develop around the QSO sources as they locally heat their surroundings. The sizes of these heated regions depend strongly on the spectra of the QSOs, with the harder spectrum S2 yielding noticeably more widespread heating. These regions are initially rare, but as more QSO sources form, they begin to overlap and bring the higher density regions into emission. Eventually, the QSOs become sufficiently numerous to heat the voids, and the entire simulation volume transitions into emission at $z \sim 9.5$ and 9 for S2 and S3, respectively. In S2 and S3, early ionized bubbles are less sharply outlined, since the δT_{b} is closer to zero than it is in the other simulations.

The X-ray heating in S2 and S3 is larger than that predicted in some earlier works. For example, Eide et al. (2018) find a negligible contribution to long-range heating from their QSO source model (referred in their paper as BH). Contrarily, the predictions from Yajima & Li (2014) and Datta et al. (2016) are more in agreement with our findings, both finding a more significant amount of X-ray heating for their single QSO.

In S4 and S5, the long-range X-ray heating due to HMXBs produces an earlier and less extended transition from absorption into emission at $z \sim 14.5$ when compared to the QSO-only models (S2 and S3). Before temperature saturation is reached ($z \approx 13.5$), large-scale fluctuations throughout both S4 and S5 can be seen. These initial emission regions expand quickly, some increasing to tens of Mpc in size by $z \sim 15.5$. Additional heated regions are visible in S5 at $z \approx 16$ where QSOs have formed; however, the transition from absorption to emission and temperature saturation happens at roughly the same time in these two models, as the heating from HMXBs dominates over that from the rare QSOs. These two cases follow a similar evolution to the results found in Mesinger et al. (2013) with X-ray efficiency $f_x = 1$, although significant reionization begins earlier in their model. On the other hand Semelin et al. (2017) find that, in all models, their signals transition to emission much later and is much more patchy than our model due to their rarer sources.

In Fig. 4, smoothed mean-subtracted maps of the 21-cm signal are displayed. To generate these maps coeval cubes are smoothed in the two angular directions with a two-dimensional Gaussian beam with a FWHM corresponding to a 1.2 km baseline at the frequency corresponding to the redshift of interest ($\theta_{\text{FWHM}} = 0.221(1+z)/1200$). This maximum baseline length approximately corresponds to the planned size of the core of SKA1-Low. Along the line-of-sight (frequency) direction, the data is smoothed with a top-hat function, the width of which is equal to the co-moving

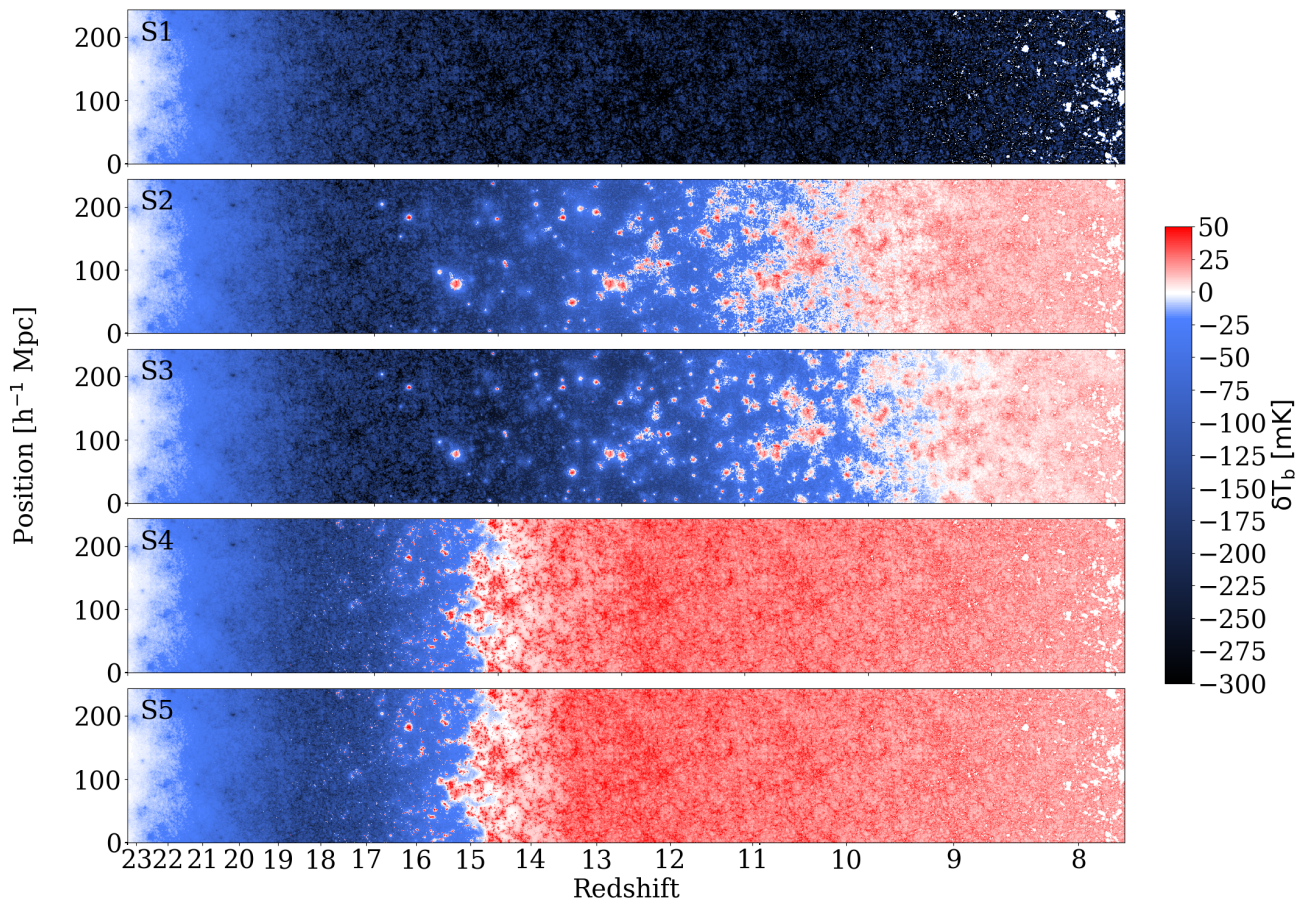


Figure 3. The position-redshift lightcone of δT_b from the five different simulations considered in this study. Here, we can see the different geometries, evolutions, and timings produced by the different source models. The details of the source models are given in Table 1. These lightcones are for the case of late Lyman- α saturation.

distance corresponding to θ_{FWHM} . Table 2 lists the angular resolution together with the expected rms noise value at this resolution for three representative redshifts.

At $z \sim 16$, the SKA1-Low noise levels for deep integrations and our standard resolution are expected to be around 5 mK. From the first column of Fig. reffig:blurred we can see that all our simulations show fluctuations that exceed this value. S4 and S5 exhibit peak fluctuations around 20 mK, and S2 and S3 have even higher ones, reaching over 40 mK in magnitude, at lower redshifts. These levels imply that each of these X-ray source models could possibly be imaged directly with SKA1-Low. Models including HMXBs, S4 and S5, then approach temperature saturation and become indistinguishable from each other after $z \sim 15$. Before this, heating from QSOs could be seen in S5, in agreement with Yajima & Li (2014) and Datta et al. (2016), which both conclude that their single QSO source may be detectable by SKA due to the large emission region it produces.

Fig. 4 shows that all our models can be distinguished visually at $z \sim 16$, showing the sensitivity of the 21-cm signal from the CD to the presence different sources. However, it should be noted that we have only explored a very small part of the enormous parameter space and there may well be degeneracy between the source parameters and the 21-cm signal they produce. For example, different

combinations of emissivities and X-ray spectra for the same source types could feasibly produce indistinguishable 21-cm maps.

In Fig. 5, we show the evolution of the mean δT_b (top panels) and its rms fluctuations, smoothed to the expected SKA resolution (bottom panels) for both early (left panels) and late (right panels) Lyman- α saturation. In all cases, we also include the high- T_b limit case, indicating when the temperature saturation limit is being approached.

When we assume Lyman- α saturation (top left panel), all simulations start in absorption due to the initially very cold IGM. In S1, the IGM remains cold and thus $\overline{\delta T_b}$ decreases all the way to $z \sim 11$ when the highest density peaks start to become ionized and cause the signal to increase slightly.

The signal in S2 and S3 initially follows a similar pattern; however, after redshift $z \approx 17$, heating from the QSOs begins to have an impact and gradually raises the temperature of the neutral IGM until it eventually asymptotes to the high-temperature limit at $z \approx 8-9$. The more energetic QSOs in S2 contribute more to heating and produce a weaker absorption signal and earlier transition to emission than those in S3. The presence of HMXBs has a much greater impact on the global mean than the QSOs for the models chosen here. Consequently, the mean value from S4 begins to increase markedly earlier and follows a pattern more similar to that seen in Mesinger et al. (2013). Our models predict that the value

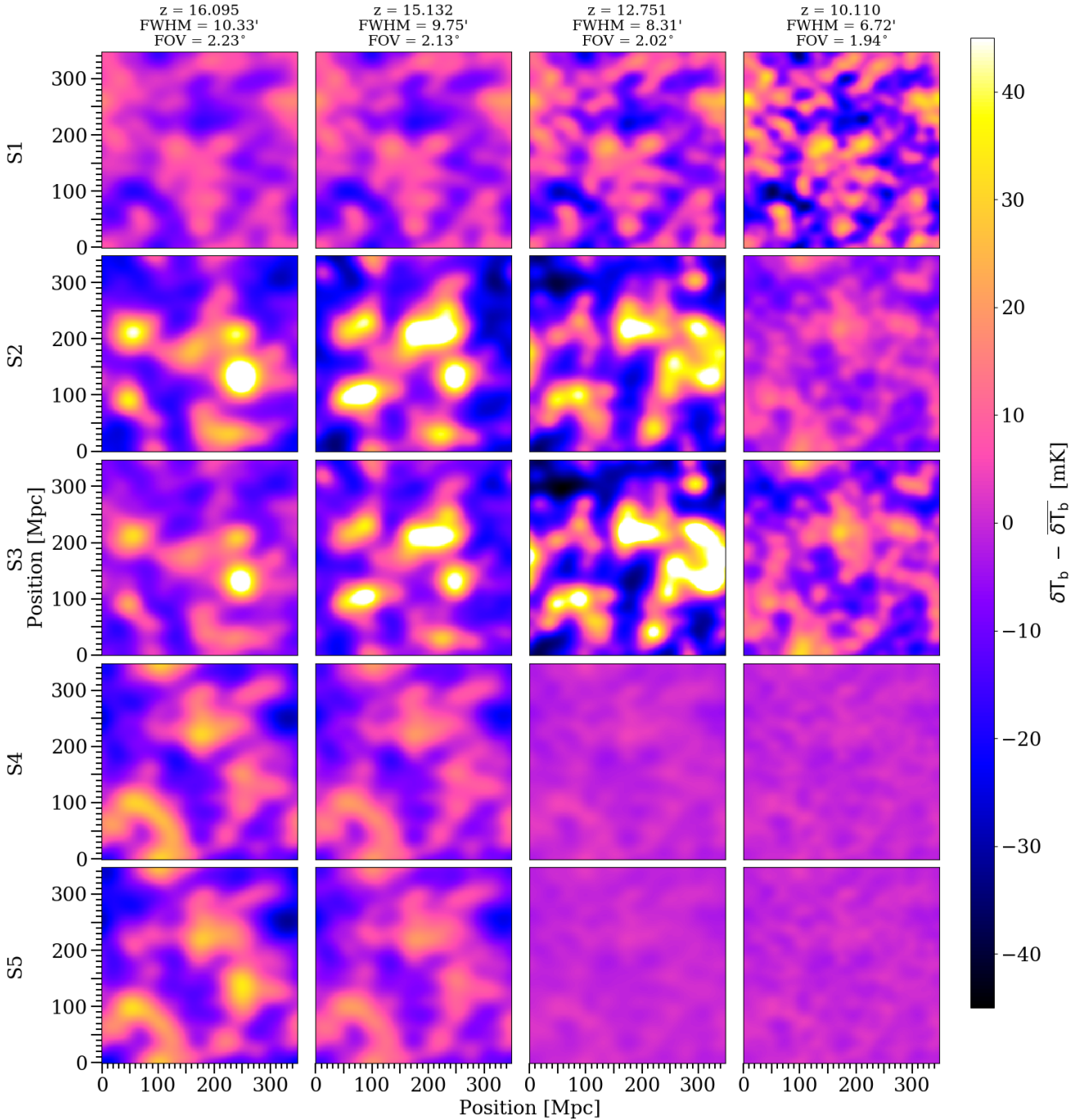


Figure 4. Mean-subtracted δT_b maps, smoothed with a Gaussian beam with a FWHM corresponding to a 1.2 km maximum baseline at the relevant frequency and bandwidth-smoothed with a top hat function (width equal to the distance corresponding to the beam width). The rows correspond to our five models. The columns represent higher to lower redshift from left to right.

of $\overline{\delta T_b}$ rises significantly earlier than all models shown in Semelin et al. (2017), again due to the relative rarity of their X-ray sources.

In the case of late Lyman- α saturation (top right panel), $\overline{\delta T_b}$ instead starts at zero, as the Lyman- α coupling is inefficient at these early times. This mean value then decreases to meet the fully coupled cases, as the Lyman- α background appreciates. Late Lyman- α coupling considerably reduces the length of the period of strong absorption compared to the case of early Lyman- α saturation. The ab-

sorption signal peak magnitude is noticeably reduced in the early-heating cases S4 and S5. In contrast, the magnitude is unaffected in the late-heating cases, as Lyman- α saturation is achieved before the absorption signal peaks. Semelin et al. (2017) find that their rarer sources produce a Lyman- α background that saturates much more gradually.

The lower panels of Fig. 5 show the rms (i.e. the standard deviation) of δT_b , smoothed to the expected resolution of SKA. The

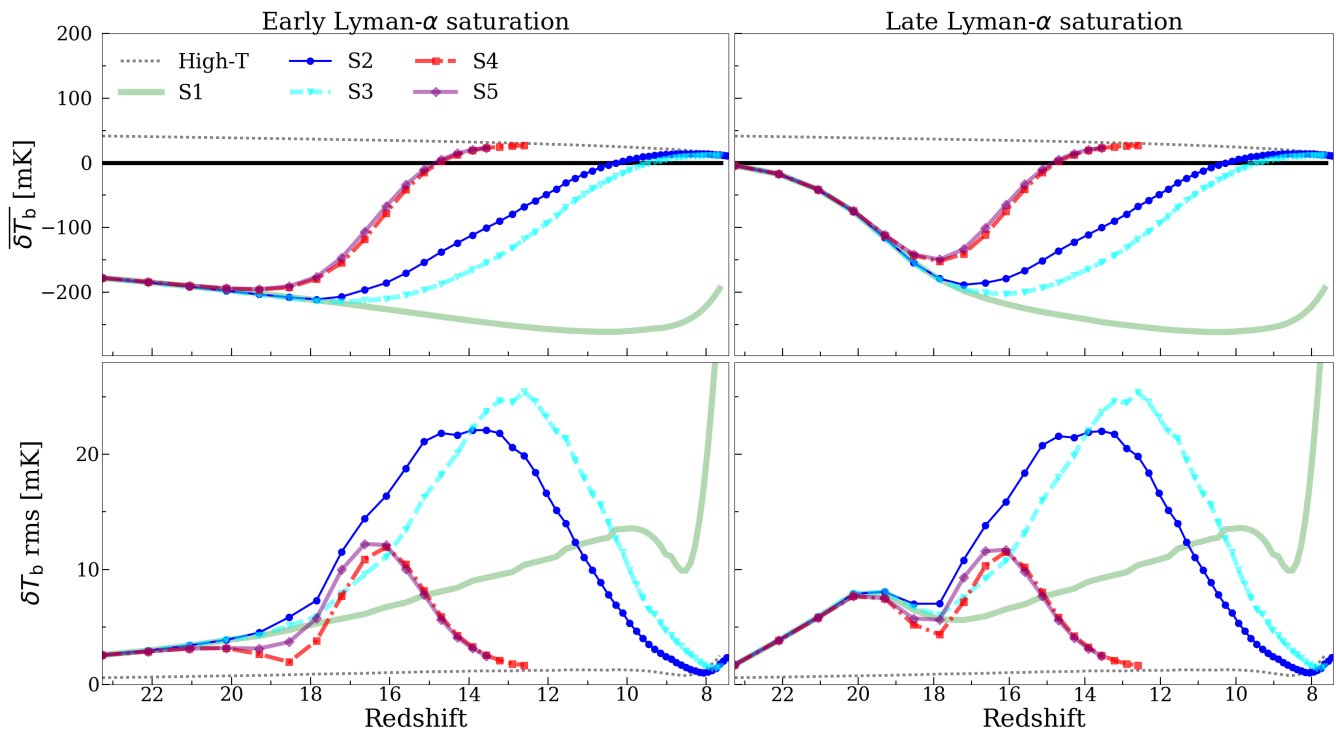


Figure 5. The mean and rms of δT_b for both early Lyman- α saturation (left-hand panels) and late Lyman- α saturation (right-hand panels). The high- T_S limit is shown to illustrate when temperature saturation occurs in each model.

lower left-hand panel of Fig. 5 displays the rms calculated for the case of early Lyman- α saturation. Before the X-ray heating is able to have significant impact on the cold IGM, all scenarios follow a similar rms evolution, which is dominated by the density fluctuations and the adiabatic cooling of the IGM. The fluctuations in S1 continue to be driven by density fluctuations, which increase as structure formation progresses. At $z \sim 10$, ionized bubbles begin to grow around the sources, increasing δT_b in dense regions near sources. As the deep absorption signals from these dense regions become weaker the rms decreases. As these bubbles continue to expand, δT_b approaches zero in increasingly large regions around the sources, contrasting with the signal from the neutral IGM and increasing the rms. The high- T_S limit follows the same evolution, but the rms fluctuations are much lower due to the signal being assumed to be in emission rather than absorption.

The rareness of QSOs in S2 and S3 introduces large-scale heating fluctuations, which increase the peak rms values by a factor of about two compared to S4 and S5, before the rms decreases in all heating scenarios as heating saturation is approached. The softer QSO model S3 peaks somewhat later than S2 as the harder QSOs produce more energy in our models. The additional heating fluctuations due to the QSOs yield a slightly earlier rms fluctuations peak in S5 ($z \approx 16.5$) compared to S4 ($z \approx 16$).

In all simulations, the inclusion of the inhomogeneous Lyman- α (Fig. 5, bottom right) background boosts the early fluctuations, which results in an additional peak in the rms at $z \sim 20$. These additional fluctuations come from inhomogeneities in the Lyman- α background being introduced into the signal. Fluctuations at later times ($z < 18$) are unaffected, since the Lyman- α background saturates.

5.3 Power Spectra

In Fig. 6, we show the power spectra of δT_b at several key redshifts along with the error on the power spectra due to noise (calculated as outlined in Villaescusa-Navarro et al. (2014)). At the beginning of the simulation ($z \sim 22$), all simulations give identical results with very high (absorption) signal for early Lyman- α saturation and very low signal for late Lyman- α coupling, since in the latter case, the 21-cm signal is still coupled to T_{CMB} . At this stage, the heating has not yet had a significant impact. Thus in the early Lyman- α saturation cases, the 21-cm fluctuations simply follow the density ones, with a boost due to the strong absorption compared to the high- T_S limit.

If the Lyman- α background has not yet saturated, the power is suppressed on all scales. As the Lyman- α couples to the CMB in the regions close to the stars first, the large distances between these regions boost the power on large scales. However, this conclusion appears dependent on the Lyman- α model employed. Early work (Santos et al. 2008) found the opposite effect. However, model S7 in Baek et al. (2010) yields a power spectra with a similar shape to ours, albeit with more power especially on smaller scales. As they have plotted power spectra as a function of x_α rather than redshift this difference in magnitude could be due to comparing different redshifts.

By $z \sim 20$, Lyman- α coupling has become efficient in the late Lyman- α saturation case. The power has increased on all scales compared to the beginning of the simulation, particularly the very large scales. There is more power at large scales in the late Lyman- α saturation case than the early Lyman- α saturation case due to the large-scale fluctuations introduced by the inhomogeneous Lyman- α background.

Santos et al. (2008) find the inverse to this, with fluctuations

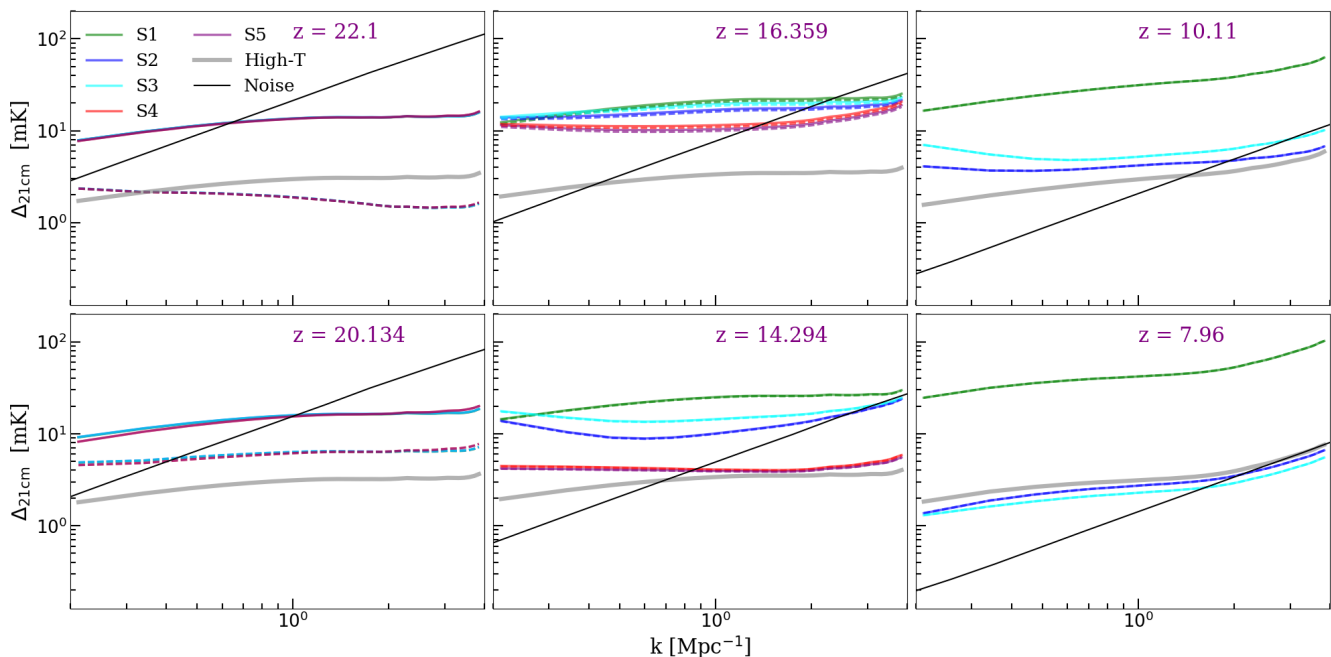


Figure 6. The 21-cm power spectra from our simulations at several key stages of the evolution assuming early (solid lines) and late (dashed lines) Lyman- α saturation. For reference, the high- T_S limit is indicated, as labeled. The error due to noise is also included (straight lines, as labelled).

from Lyman- α being introduced on small rather than large scales at this redshift. Pritchard & Furlanetto (2007) find that Lyman- α fluctuations dominate at this stage, due to the different timing of their models. In the case of late Lyman- α saturation, the models remain almost the same, with only a slight difference between the models with and without HMXBs. Santos et al. (2008) find comparable results to our own. Due to the different timings of the models, it is difficult to compare to the results of Semelin et al. (2017). We compare this redshift to their power spectra from $z \approx 10$ (where their heating has just begun and Lyman- α is not yet fully coupled). These power spectra agree on large scales, but we find somewhat more power on smaller scales. This is likely due to the presence of more less massive sources in our simulations, as they introduce fluctuations on smaller scales.

By $z \approx 16$, the Lyman- α background is sufficiently built up so that the early and late Lyman- α saturation results converge. This is somewhat earlier than found in Santos et al. (2008), where Lyman- α saturation does not occur until $z \approx 10$. The small-scale power in simulations S4 and S5 begins to decrease, as X-ray heating washes out small-scale temperature fluctuations; whereas on larger scales, the power is slightly boosted for the same reason. S2 and S3 follow a similar pattern, but have more power on large scales due to the rareness of the brighter QSOs. On smaller scales, they also have more power, as significant heating has not extended to much of the simulation and hence has not washed out the small-scale temperature fluctuations from previous QSO activity. Both Santos et al. (2008) and Baek et al. (2010) find power spectra with a similar magnitude and shape at this time, but with a peak at smaller scales than those found here.

By $z \approx 14$, the 21-cm power is near its peak in S2 and S3 due to large-scale heating fluctuations, introducing strong contrast between the hot and cold regions. The power is starting to decline significantly in S4 and S5. As the transition to emission takes place,

convergence to the high- T_S limit (which can then be used to describe the rest of the EoR accurately) is approached. The power in S2 and S3 is still boosted on large scales compared to that of S1, but long-range heating is beginning to suppress the power on smaller scales.

At $z \approx 10$, S4 and S5 have reached temperature saturation. These models are in rough agreement with the power spectra found in Santos et al. (2008). S3 and S4 approach temperature saturation much more gradually and later ($z \approx 7.9$), with slightly more power remaining in large-scale fluctuations. S3 evolves more slowly than S2 due to the QSOs producing less energy in this model, thus heating more locally. Power on all scales in S2 and S3 is lower than in the high- T_S case, as reionization has begun. Regions of the simulation that are transitioning from absorption to emission have values closer to the zero-signal coming from ionized regions, which decreases the magnitude of the fluctuations. In the fully saturated case, there is more contrast between the emission signal from heated, neutral regions and zero signal from ionized regions, so the magnitude of fluctuations is greater.

The redshift evolution of several k -modes are shown in Fig. 7. Panels on the left-hand side show results from the early Lyman- α heating. On large scales, X-ray heating from HXMBs initially suppresses fluctuations, as heating weakens the absorption signal from the densest regions around sources. As these regions move towards emission, the large-scale fluctuations are boosted before decreasing once more, as temperature saturation approaches. When in combination with HMXBs, QSOs follow a similar pattern. However, with QSOs alone, there is no trough present as many high density regions remain in strong absorption due to the rarity of the QSOs.

The evolution on smaller scales is somewhat similar, however, at no point are the fluctuations boosted by X-ray heating. The removal of deep absorption signals from dense regions around sources causes this decrease in power, occurring more rapidly in

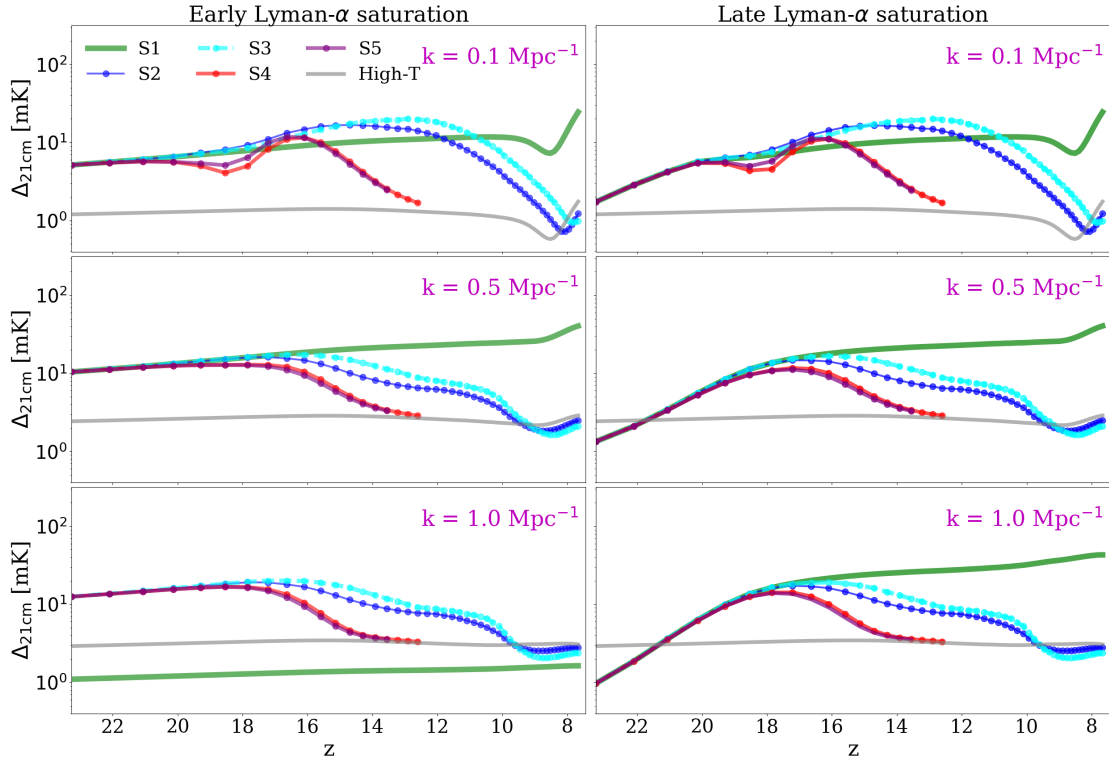


Figure 7. The evolution of the 21-cm power spectra modes at $k = 0.1, 0.5,$ and 1 Mpc^{-1} for all X-ray source models. On the left-hand side panels, power spectra modes from the early Lyman- α saturation scenario are displayed, and on the right, the late Lyman- α saturation. The high- T_S limit is displayed to illustrate temperature saturation.

models with HMXBs as X-rays are emitted from each halo. Power on small scales is suppressed more rapidly in S2, as long-range heating is more significant.

Fluctuations including the inhomogeneous Lyman- α background from late Lyman- α saturation are shown in the right-hand panels. Initially, fluctuations are suppressed in all models until the Lyman- α background has been established. This Lyman- α case particularly impacts the fluctuations in S4 and S5, decreasing the peak value at $z = 16$ to $\log_{10}(\Delta_{21\text{cm}}) \approx 0.9$. The peak values of S2 and S3 occur later, after Lyman- α saturation is reached and so are unaffected.

5.4 Non-Gaussianity of the 21-cm signal

The power spectra alone cannot be used to fully describe δT_b fluctuations from X-ray heating as they are highly non-Gaussian. Therefore, we consider the higher moments (skewness and kurtosis) of the one-point statistics of the 21-cm signal produced from our simulations. We use the following dimensionless definitions for skewness and kurtosis:

$$\text{Skewness}(y) = \frac{1}{N} \frac{\sum_{i=0}^N (y_i - \bar{y})^3}{\sigma^3}, \quad (9)$$

and

$$\text{Kurtosis}(y) = \frac{1}{N} \frac{\sum_{i=0}^N (y_i - \bar{y})^4}{\sigma^4}. \quad (10)$$

Here, y is the quantity of interest (i.e., δT_b), N is the total number of data points, and \bar{y} and σ^2 are the mean and variance of y , respectively. These quantities are all smoothed to the resolution of SKA1-Low and are calculated from coeval simulation boxes. The fact that QSO sources are stochastic and do not trace the Gaussian density distribution leads to a dramatic increase in non-Gaussianity. Therefore, compared to the other measures discussed, these higher order statistics demonstrate the most extreme differences between models with and without QSOs.

In Fig. 8, we show the evolution of the skewness (top) and kurtosis (bottom) for both early (left) and late (right) Lyman- α saturation. S1 shows a flat, featureless evolution throughout the CD, since the density field at early times is close to Gaussian. The skewness only increases once significant reionization begins at $z \sim 10$, when stars ionize the high-density peaks. These ionized regions introduce non-Gaussianity into the signal, as shown in previous studies (Mellema et al. 2006).

In all cases with X-ray heating, the skewness initially follows that of S1 until $z \sim 20$ when QSOs begin to form in S2, S3, and S5. In the hard-spectra QSO cases S2 and S5, the skewness increases rapidly; while in the softer-spectrum case S3, it increases

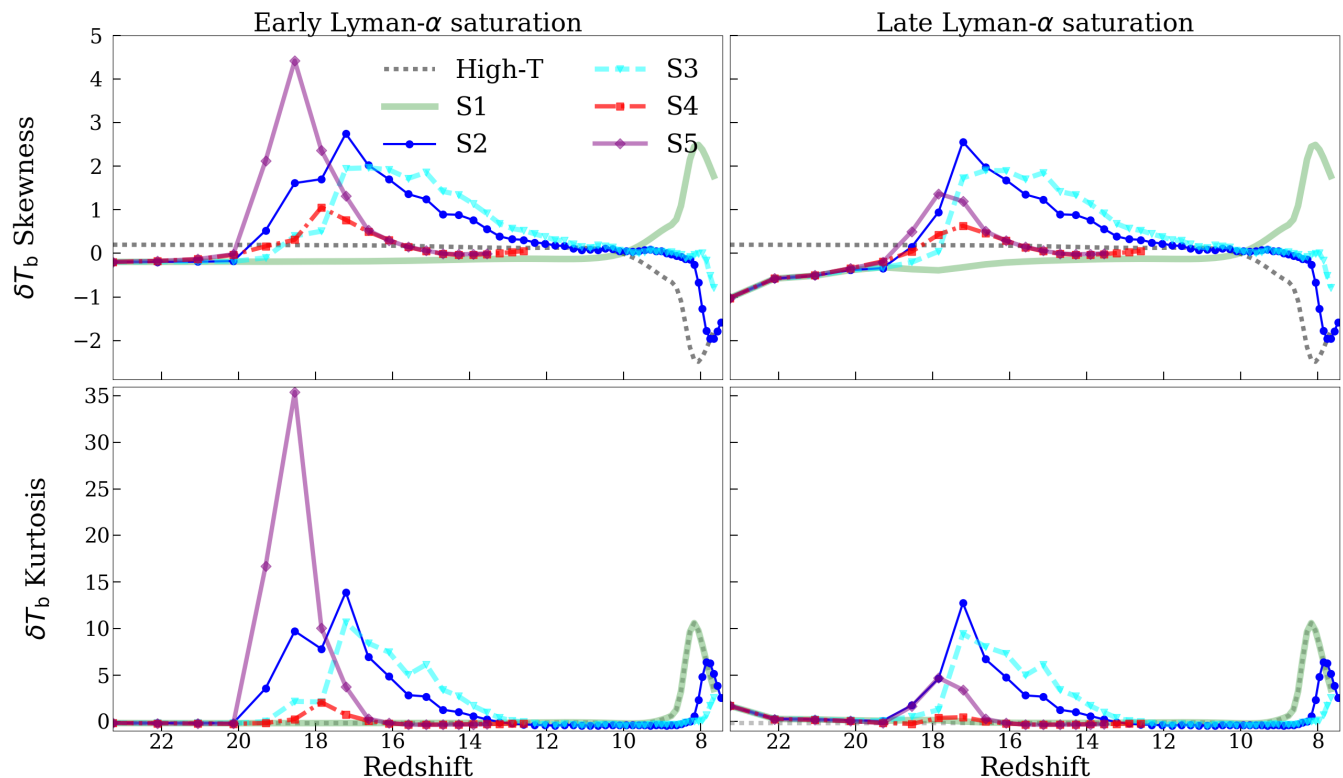


Figure 8. The evolution of the skewness (top panels) and kurtosis (bottom panels) of δT_b for all simulations, as labeled, for early Lyman- α saturation (left panels) and late one (right panels).

more gradually. Similarly in S4, the skewness increases gradually (and peaks at a lower value), since non-Gaussianities are added by the (softer-spectrum) HMXBs. The maximal skewness from S5 is 4.5, or over four times greater than the value (~ 1) obtained from S4. The peak in S5 also occurs somewhat earlier, at $z \sim 18.5$ rather than $z \sim 18$. The maximal skewness values obtained from S2 (2.7) and S3 (2.0) are intermediate between those from S4 and S5, while still much higher (by factors of 27 and 20, respectively) than the value found for S1 (0.1). The largest value for S2 occurs earlier (at $z \sim 17.5$) than that of S3 ($z \sim 16$), as the harder QSOs heat more rapidly the cold IGM patches responsible for driving the 21-cm signal fluctuations.

The inhomogeneous Lyman- α background (Fig. 8, right panels) introduces additional non-Gaussian fluctuations of δT_b due to regions around the sources that first become decoupled from T_{CMB} . These dominate over the density fluctuations and give rise to the negative skewness observed in all cases, which then gradually increases as the Lyman- α background builds up as more of the simulation volume decouples from T_{CMB} . Thereafter ($z < 19$), heating starts, and temperature variations begin to impact the signal. In all cases, the skewness increases and eventually peaks; however in the X-ray source models where heating occurs earlier, the peaks due to heating fluctuations are suppressed compared to the early Lyman- α saturation. This suppression is particularly evident for S5.

The kurtosis (Fig. 8, lower panels) follows the same qualitative pattern, but with an even more extreme difference between the QSO and non-QSO cases. The maximal value of the kurtosis from S4 (~ 1) is 17 times smaller than the corresponding value from S5. The kurtosis yields a more notable difference between the two

QSO models, with S2 reaching a peak value of 14 versus 10 for S3 (both are significantly greater than the value from S1, which is close to zero). The greater amount of heating from the harder QSOs in S2 again leads to a larger deviation from Gaussian fluctuations observed.

When Lyman- α coupling is not complete before heating begins (Fig. 8, bottom right), the maximal kurtosis is also suppressed. This effect is most notable for the X-ray source models S4 and S5, where heating occurs earlier, with the peak in S4 being totally suppressed. The maximum value of S5 is decreased by a factor of 10. The kurtosis of S2 and S3 are slightly suppressed initially, but the largest values remain the same as they occur at lower redshift when Lyman- α is closer to saturation.

Finally, in Fig. 9 we show the skewness and kurtosis of our simulations with the addition of telescope noise using the method outlined in Ghara et al. (2017) and Giri et al. (2018). The strong non-Gaussianity in the signal is somewhat washed out, especially at out at higher redshifts. The peaks values of both the skewness and the kurtosis are lowered, particularly in the case of early Lyman- α saturation. The non-Gaussianity from reionization itself is also decreased. However, even when telescope noise is present our different Cosmic Dawn X-ray models can still be distinguished from each other.

6 CONCLUSIONS

In this paper, we present a suite of large-volume, fully numerical radiative transfer simulations of X-ray heating of the IGM during the CD, extending our previous work in Paper I. We introduced

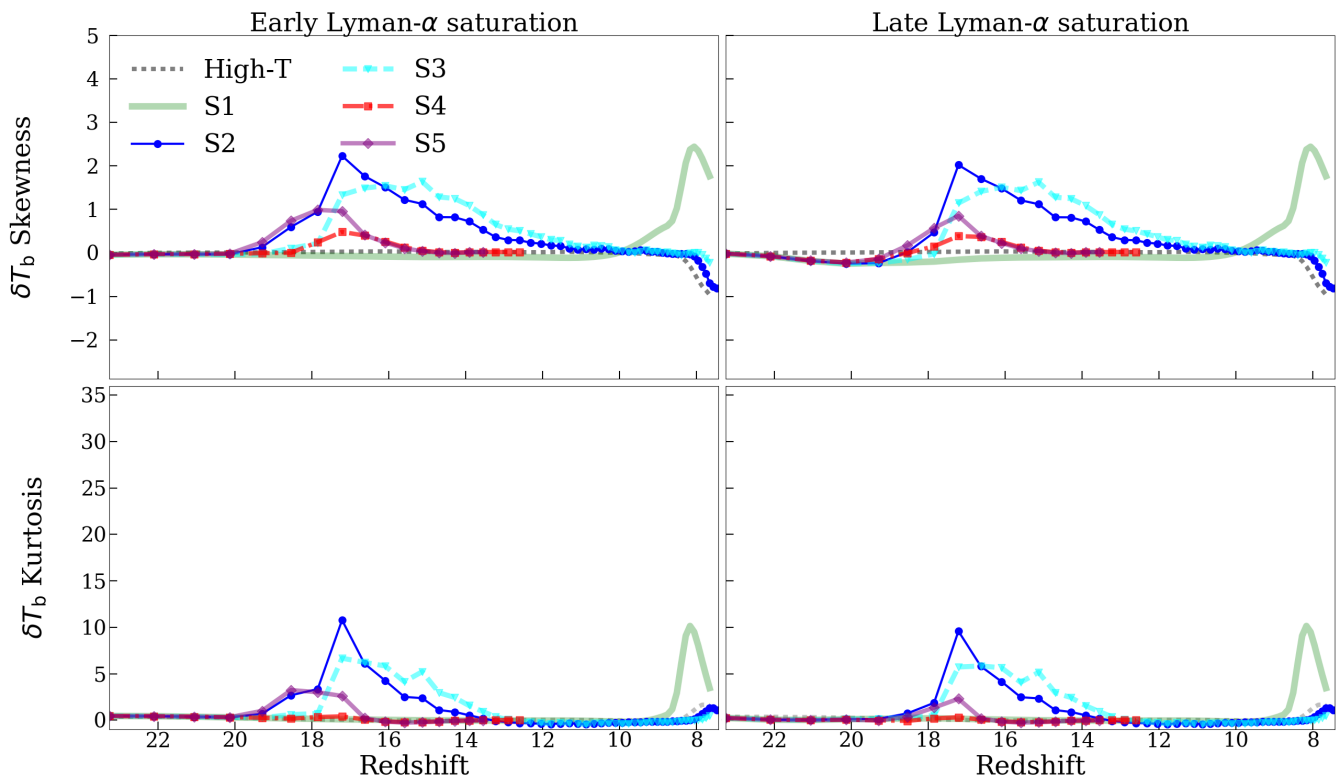


Figure 9. The evolution of the skewness (top panels) and kurtosis (bottom panels) of δT_b with telescope noise added. Results from all simulations are shown for early Lyman- α saturation (left panels) and late one (right panels).

two types of QSO sources, with power-law spectral slopes of -0.8 and -1.6, and compare their impact to the effects of HMXB X-ray sources considered in Paper I, as well as a new case combining QSO and HMXB sources and a fiducial, stars-only simulation. Unlike HMXBs, the QSOs are rare and are assigned randomly to HMACH haloes with luminosities sampled from the high-redshift extrapolation of an empirical QXLF. These luminosities are not proportional to the host halo mass. As the precise nature and properties of these early sources remain uncertain, we have chosen a QXLF that predicts fairly numerous QSOs in order to examine their maximum possible impact. Our simulations show QSO sources may be able to contribute non-trivially to early X-ray heating and also suggest that it is possible to distinguish between soft- and hard-spectra models using the resulting 21-cm signal, particularly via the non-Gaussianity of the signal.

These QSO sources contribute many fewer photons to the X-ray heating than HMXBs, so their overall energy contribution is subdominant compared to HMXB sources when both source types are present. On their own, both QSOs models yield a considerably more extended transition of the 21-cm signal from absorption to emission, and spin temperature saturation of the neutral IGM is not reached until reionization itself is well under way. The late temperature saturation in the simulations with only QSOs cause the non-Gaussianity from reionization itself ($z < 10$) to be lower than in the case of full saturation of the spin temperature. This effect is more pronounced for the QSOs with softer X-ray spectra.

During the CD, heating from QSOs has a more notable impact on the heating fluctuations than on the mean value of δT_b . When compared to the stellar-only case, the δT_b power spectrum from all X-ray models show more power on larger scales and less

on smaller scales until around $z \sim 16$. After this time, the power spectrum of simulations including HMXBs decreases on all scales as temperature saturation is approached, but the power spectra for the QSO cases experience a further boost on large scales. The rms fluctuations for all X-ray source models are above the expected noise levels for observations with the SKA1-Low core, implying that low resolution tomographic imaging of the CD may be possible. The rare QSOs boost the rms, particularly when they are the only sources of X-ray heating. In this case, the peak value of the fluctuations are ~ 10 mK higher than in the HMXB cases, and this peak occurs at lower redshift.

By far, the clearest signature of the QSOs is found in one-point higher order statistics of the 21-cm signal PDF distribution: skewness and kurtosis. An increase in both quantities can be seen both when QSOs are the sole sources driving X-ray heating and when they are present with HMXBs. These strong non-Gaussianities are driven by the rareness of the QSOs, introducing fluctuations in the signal largely unrelated to the underlying (mostly Gaussian) density field. However, this increase in non-Gaussianity can be partly suppressed by late Lyman- α saturation, so while an extremely non-Gaussian signal from the CD could indicate the presence of QSOs, a more Gaussian signal would not rule them out.

In addition to suppressing the non-Gaussianities, the Lyman- α background fluctuations (in all models) produced by late Lyman- α saturation cause an additional peak in δT_b fluctuations, as has been found in several previous works (e.g. Santos et al. 2008; Baek et al. 2010; Ghara et al. 2015; Watkinson & Pritchard 2015). The power spectra show that this is due mainly to contribution from larger scales. The peak magnitude of these rms fluctuations driven by the Lyman- α background is ≈ 8 mK, which is well below the

expected image noise of 20 mK for imaging with the SKA1-Low core. However, a power spectrum detection of these fluctuations should still be possible.

The difference found between our work and that in [Eide et al. \(2018\)](#) is model dependent and is in part due to their seeding algorithm only allowing the formation of black holes in haloes greater than $10^{10}M_{\odot}$, resulting in a much lower number density of QSOs. This lower density combined with the assumption that QSOs have optically thick, geometrically thin disks (as described in [Shakura & Sunyaev \(1973\)](#)) leads to a somewhat more conservative heating prediction than in our models. This is illustrated by our agreement with [Yajima & Li \(2014\)](#), who follow a prescription similar to [Eide et al. \(2018\)](#) but assumes that black holes accrete at their Eddington luminosities. [Datta et al. \(2016\)](#) also predict that their individual, bright QSO would be detectable in 1000 h integrations with SKA1-Low – which is in agreement with our own predictions. [Datta et al. \(2016\)](#) use observations of the low-redshift QSOs to determine their luminosities, a method more comparable to our own.

A key implication of the results presented in this work is that all the X-ray source models we investigated go through phases in which the fluctuations in the 21-cm signal are above the expected noise for observations with the core of SKA1-Low ([Koopmans et al. 2015](#)), suggesting that at least part of this epoch could not only be studied with power spectra, but directly imaged. In Paper I, we found this to be the case for HMXBs, and we can now extend this conclusion to the cases with rare, QSO-like sources. With higher levels of galactic foregrounds and stronger ionospheric effects, imaging around $z \sim 16$ will not be easy, but images of the CD would open the door to a multitude of analysis techniques to extract information from the signal about the astrophysics of the CD. Examples include parameter estimation through deep learning of images ([Shimabukuro & Semelin 2017](#); [Gillet et al. 2019](#), e.g.) and MCMC approaches ([Greig & Mesinger 2018](#), e.g.), emulators ([Kern et al. 2017](#), e.g.), the bispectrum ([Shimabukuro et al. 2016](#), e.g.), and size distributions of features (e.g. [Giri et al. 2018](#)).

[Ghara et al. \(2015\)](#) and [Baek et al. \(2010\)](#) find power spectra with similar magnitudes to our own. Detailed comparisons to these works are complicated by the fact that [Baek et al. \(2010\)](#) has no subgrid model for unresolved, low-mass sources and [Ghara et al. \(2015\)](#) use a subgrid model very different from the one employed in this work. The subgrid modeling is particularly important for comparisons as lower resolutions of these simulations mean that resolved haloes do not appear until later in the CD. [Pritchard & Furlanetto \(2007\)](#) and [Pacucci et al. \(2014\)](#) also find power spectra with comparable magnitudes. The large-scale fluctuations in these works (at $k \approx 0.1\text{Mpc}^{-1}$) peak at roughly the same time as our models including HMXBs.

[Baek et al. \(2010\)](#) and [Watkinson & Pritchard \(2015\)](#) include measures of the power spectra and higher order statistics of the 21-cm signal produced by HMXB sources. The peak skewness values during the CD found from models S4 and S2 in [Baek et al. \(2010\)](#) are in agreement with the ones found in our HMXB model (S4), but are significantly lower than the values found from our simulations including QSOs. The lack of correlation between our QSO luminosities and their host dark matter haloes, along with their rareness are the factors driving this. The difference is far more pronounced in the early Lyman- α saturation case, but still noticeable in the late Lyman- α saturation case. Similarly, the skewness found for all models in [Watkinson & Pritchard \(2015\)](#) have peak values far lower than that of our QSO models (but the case ‘ $\log \zeta_X = 55$ ’ is in agreement with our HMXB model).

The high level of non-Gaussianity produced by QSOs imply

that higher order statistics may be a more useful probe than the power spectra to discriminate between certain source models in the CD. In particular, high non-Gaussianity likely indicates the presence of rare sources, such as QSOs. The skewness shows a clear difference between our models including QSOs and our models containing HMXBs, as well as models from other works. Clearly our QSO-like sources introduce a significantly greater amount of non-Gaussianity in the signal. This result further motivates the use of alternative analysis techniques to interpret the signal from the CD to probe for rare X-ray sources. The bispectra of the 21-cm signals from all the X-ray simulations presented here have been extensively studied in [Watkinson et al. \(2019\)](#).

Conversely, investigating the non-Gaussianities during the EoR could be less insightful than previously hoped if late heating occurs. Despite the additional fluctuations introduced to the kinetic temperature of the gas, non-Gaussianities during the EoR are in fact lower in our QSO-only models. This decrease is due to the magnitude of δT_b from the neutral regions being lower in the late heating case than for the saturated spin temperature case, removing the brightest points from the signal.

There are some other potential X-ray sources that may have contributed to the fluctuations in the 21-cm signal in the CD that we have not yet considered, for example supernovae (e.g. [Yajima & Khochfar 2015](#)). In addition, there is still a large parameter space associated with our current sources, for example varying the star formation efficiency of haloes and hence the luminosity of our HMXBs. Due to the computational expense of our simulations, we have not yet been able to fully explore the huge parameter space associated with the CD. However, the alternative of exploring the parameter space with fast semi-numerical models may not be sufficient. Ideally, these two approaches should be combined in order to achieve reliable predictions and interpretation of any observational detections.

Another limitation of the current work is the modeling of the Lyman- α background. We have included only the two most extreme cases, one where very early sources build up a Lyman- α background before the simulation begins (early Lyman- α saturation) and one where only sources present in our simulation volume contribute to the Lyman- α background (late Lyman- α saturation). However, the most likely scenario is somewhere in between, with earlier sources, such as mini-haloes, contributing a non-negligible Lyman- α flux to the background, but not achieving full Lyman- α saturation.

Finally, recent observations suggest that the $z \approx 10$ Universe may not be as dust and metal free as previously thought ([Chiaki & Wise 2019](#); [Tamura et al. 2019](#)). Dust impacts the properties and evolution of galaxies, in particular the escape fraction, which could impact our results for this time. Our RT calculations assume hydrogen and helium to be the only elements present and may not be sufficient once enough metal enrichment has occurred. We leave these considerations for future work.

Despite these few caveats, the results from our simulations have shown that the 21-cm signal from the CD may not only be statistically detectable with SKA1-Low, but also imageable. Our X-ray source models have distinct power spectra with markedly different the evolution for our difference models. Finally, the high non-Gaussianity driven by X-ray heating illustrates the need to consider statistics beyond the power spectrum when considering this signal, particularly when considering rare X-ray sources.

7 ACKNOWLEDGEMENTS

This work was supported by the Science and Technology Facilities Council [grant numbers ST/I000976/1 and ST/P000525/1] and the Southeast Physics Network (SEPNet). GM is supported in part by Swedish Research Council grant 2016-03581. This research was supported in part by the Munich Institute for Astro- and Particle Physics (MIAPP) of the DFG cluster of excellence “Origin and Structure of the Universe”. We acknowledge that the results in this paper have been achieved using the PRACE Research Infrastructure resource Marenostrum based in the Barcelona Supercomputing Center, Spain under Tier-0 project ‘Multi-scale Reionization’. We acknowledge that some of the results of this research have been achieved using the DECI resource Cartesius based in Netherlands at SURFSara with support from the PRACE aisbl. Some of the numerical computations were done on the Apollo cluster at The University of Sussex. Part of the simulations were performed on resources provided by the Swedish National Infrastructure for Computing (SNIC) at the PDC Center for High Performance Computing in Stockholm. The N -body simulation used in this work was completed under the Partnership for Advanced Computing in Europe, PRACE, Tier-0 project PRACE4LOFAR on the TGCC Curie computer. Finally, we would like to thank the referee for helping us improve this work with their constructive comments.

REFERENCES

- Ahn K., Xu H., Norman M. L., Alvarez M. A., Wise J. H., 2015a, *ApJ*, **802**, 8
- Ahn K., Xu H., Norman M. L., Alvarez M. A., Wise J. H., 2015b, *ApJ*, **802**, 8
- Akiyama M., et al., 2018, *Publications of the Astronomical Society of Japan*, **70**, S34
- Ali Z. S., et al., 2015, *ApJ*, **809**, 61
- Ali Z. S., et al., 2018, *ApJ*, **863**, 201
- Baek S., Semelin B., Di Matteo P., Revaz Y., Combes F., 2010, *A&A*, **523**, A4
- Becker G. D., Bolton J. S., Madau P., Pettini M., Ryan-Weber E. V., Venemans B. P., 2015, *MNRAS*, **447**, 3402
- Bolton J. S., Becker G. D., Raskutti S., Wyithe J. S. B., Haehnelt M. G., Sargent W. L. W., 2012, *MNRAS*, **419**, 2880
- Borisova E., Lilly S. J., Cantalupo S., Prochaska J. X., Rakic O., Worseck G., 2016, *ApJ*, **830**, 120
- Bosman S. E. I., Fan X., Jiang L., Reed S., Matsuoka Y., Becker G., Haehnelt M., 2018, *MNRAS*, **479**, 1055
- Bowler R., 2014, Unveiling the merger fraction, sizes and morphologies of the brightest $z \sim 7$ galaxies, HST Proposal
- Bowler R. A. A., et al., 2012, *MNRAS*, **426**, 2772
- Bowler R. A. A., et al., 2015, *MNRAS*, **452**, 1817
- Bowman J. D., Rogers A. E. E., Monsalve R. A., Mozdzen T. J., Mahesh N., 2018, *Nature*, **555**, 67
- Brightman M., et al., 2013, *MNRAS*, **433**, 2485
- Chardin J., Haehnelt M. G., Aubert D., Puchwein E., 2015, *MNRAS*, **453**, 2943
- Chen K.-J., Bromm V., Heger A., Jeon M., Woosley S., 2015, *ApJ*, **802**, 13
- Chiaki G., Wise J. H., 2019, *MNRAS*, **482**, 3933
- Chisholm J., et al., 2018, *Astronomy and Astrophysics*, **616**, A30
- Das A., Mesinger A., Pallottini A., Ferrara A., Wise J. H., 2017, *MNRAS*, **469**, 1166
- Datta K. K., Ghara R., Majumdar S., Choudhury T. R., Bharadwaj S., Roy H., Datta A., 2016, *Journal of Astrophysics and Astronomy*, **37**, 27
- Davies F. B., Hennawi J. F., Eilers A.-C., Lukić Z., 2018, *ApJ*, **855**, 106
- Dawoodbhoj T., et al., 2018, *MNRAS*, **480**, 1740
- De Barros S., et al., 2017, *A&A*, **608**, A123
- Dijkstra M., Haian Z., Rees M. J., Weinberg D. H., 2004, *ApJ*, **601**, 666
- Dixon K. L., Iliev I. T., Mellema G., Ahn K., Shapiro P. R., 2016, *MNRAS*, **456**, 3011
- Douna V. M., Pellizza L. J., Laurent P., Mirabel I. F., 2018, *MNRAS*, **474**, 3488
- Efstathiou G., 1992, *MNRAS*, **256**, 43P
- Eide M. B., Graziani L., Ciardi B., Feng Y., Kakiichi K., Di Matteo T., 2018, *MNRAS*, **476**, 1174
- Fialkov A., Barkana R., Visbal E., 2014, *Nature*, **506**, 197
- Field G. B., 1958, *Proceedings of the IRE*, **46**, 240
- Fioc M., Rocca-Volmerange B., 1999, ArXiv Astrophysics e-prints,
- Friedrich M. M., Mellema G., Iliev I. T., Shapiro P. R., 2012, *MNRAS*, **421**, 2232
- Furlanetto S. R., Hernquist L., Zaldarriaga M., 2004, *MNRAS*, **354**, 695
- Ghara R., Choudhury T. R., Datta K. K., 2015, *MNRAS*, **447**, 1806
- Ghara R., Choudhury T. R., Datta K. K., 2016, *MNRAS*, **460**, 827
- Ghara R., Choudhury T. R., Datta K. K., Choudhuri S., 2017, *MNRAS*, **464**, 2234
- Giallongo E., et al., 2015, *A&A*, **578**, A83
- Gillet N., Mesinger A., Greig B., Liu A., Ucci G., 2019, *MNRAS*, **484**, 282
- Giri S. K., Mellema G., Dixon K. L., Iliev I. T., 2018, *MNRAS*, **473**, 2949
- Glover S. C. O., Brand P. W. J. L., 2003, *MNRAS*, **340**, 210
- Greig B., Mesinger A., 2018, in Jelić V., van der Hulst T., eds, *IAU Symposium Vol. 333, Peering towards Cosmic Dawn*. pp 18–21 ([arXiv:1705.03471](https://arxiv.org/abs/1705.03471)), doi:10.1017/S1743921317011103
- Greiner J., et al., 2009, *ApJ*, **693**, 1610
- Grissom R. L., Ballantyne D. R., Wise J. H., 2014, *Astronomy and Astrophysics*, **561**, A90
- Halpern J. P., 1984, *ApJ*, **281**, 90
- Håring N., Rix H.-W., 2004, *ApJL*, **604**, L89
- Harnois-Déraps J., Pen U.-L., Iliev I. T., Merz H., Emberson J. D., Desjacques V., 2013, *MNRAS*, **436**, 540
- Hasegawa K., Semelin B., 2013, *MNRAS*, **428**, 154
- Hassan S., Davé R., Mitra S., Finlator K., Ciardi B., Santos M. G., 2018, *MNRAS*, **473**, 227
- Higgins J., Meiksin A., 2012, *MNRAS*, **426**, 2380
- Hill J. C., Baxter E. J., 2018, *J. Cosmology Astropart. Phys.*, **8**, 037
- Iliev I. T., Mellema G., Shapiro P. R., Pen U.-L., 2007, *MNRAS*, **376**, 534
- Jeon M., Pawlik A. H., Bromm V., Milosavljević M., 2014, *MNRAS*, **440**, 3778
- Jin C., Done C., Ward M., 2017, *MNRAS*, **468**, 3663
- Kakiichi K., Graziani L., Ciardi B., Meiksin A., Compostella M., Eide M. B., Zaroubi S., 2017, *MNRAS*, **468**, 3718
- Kern N. S., Liu A., Parsons A. R., Mesinger A., Greig B., 2017, *ApJ*, **848**, 23
- Khairé V., Srianand R., Choudhury T. R., Gaikwad P., 2016, *MNRAS*, **457**, 4051
- Khrykin I. S., Hennawi J. F., McQuinn M., 2017, *ApJ*, **838**, 96
- Kneivt G., Wynn G. A., Power C., Bolton J. S., 2014, *MNRAS*, **445**, 2034
- Komatsu E., Smith K. M., Dunkley J., Bennett C. L., 2011, *ApJS*, **192**, 18
- Koopmans L., et al., 2015, *Advancing Astrophysics with the Square Kilometre Array (AASKA14)*, p. 1
- Laporte N., et al., 2017, *ApJL*, **837**, L21
- Läsker R., Greene J. E., Seth A., van de Ven G., Braatz J. A., Henkel C., Lo K. Y., 2016, *ApJ*, **825**, 3
- Lutovinov A., Revnivtsev M., Gilfanov M., Shtykovskiy P., Molkov S., Sunyaev R., 2005, *A&A*, **444**, 821
- Mainali R., Kollmeier J. A., Stark D. P., Simcoe R. A., Walth G., Newman A. B., Miller D. R., 2017, *ApJL*, **836**, L14
- Mason C. A., Treu T., Dijkstra M., Mesinger A., Trenti M., Pentericci L., de Barros S., Vanzella E., 2018, *ApJ*, **856**, 2
- McGreer I. D., Mesinger A., D’Odorico V., 2015, *MNRAS*, **447**, 499
- Mellema G., Iliev I. T., Alvarez M. A., Shapiro P. R., 2006, *Elsevier Science*, **11**, 374
- Mesinger A., Ferrara A., Spiegel D. S., 2013, *MNRAS*, **431**, 621
- Middei R., Vagnetti F., Bianchi S., La Franca F., Paolillo M., Ursini F., 2017, *A&A*, **599**, A82
- Mineo S., Gilfanov M., Sunyaev R., 2012, *MNRAS*, **419**, 2095
- Mitra S., Choudhury T. R., Ferrara A., 2018, *MNRAS*, **473**, 1416

- Mortlock D. J., et al., 2011, *Nature*, 474, 616
- Navarro J. F., Steinmetz M., 1997, *ApJ*, 478, 13
- Oñorbe J., Hennawi J. F., Lukić Z., Walther M., 2017, *ApJ*, 847, 63
- Ocvirk P., et al., 2016, *MNRAS*, 463, 1462
- Ocvirk P., et al., 2018, arXiv e-prints,
- Onoue M., et al., 2017, *ApJL*, 847, L15
- Paciga G., et al., 2011, *MNRAS*, 413, 1174
- Paciga G., et al., 2013, *MNRAS*, 433, 639
- Pacucci F., Mesinger A., Mineo S., Ferrara A., 2014, *MNRAS*, 443, 678
- Pan H. C., Stewart G. C., Pounds K. A., 1990, *MNRAS*, 242, 177
- Parsa S., Dunlop J. S., McLure R. J., 2018, *MNRAS*, 474, 2904
- Patil A. H., et al., 2017, *ApJ*, 838, 65
- Pentericci L., et al., 2014, *ApJ*, 793, 113
- Planck Collaboration 2016, *A&A*, 596, A108
- Planck Collaboration et al., 2015, ArXiv e-prints 1502.01589,
- Pritchard J. R., Furlanetto S. R., 2007, *MNRAS*, 376, 1680
- Qin Y., et al., 2017, *MNRAS*, 472, 2009
- Raskutti S., Bolton J. S., Wyithe J. S. B., Becker G. D., 2012, *MNRAS*, 421, 1969
- Ross H. E., Dixon K. L., Iliev I. T., Mellema G., 2017, *MNRAS*, 468, 3785
- Ross H. E., Dixon K., Iliev I., Mellema G., 2018, in Jelić V., van der Hulst T., eds, IAU Symposium Vol. 333, IAU Symposium. pp 34–38 (arXiv:1801.06527), doi:10.1017/S1743921317011115
- Santos M. G., Amblard A., Pritchard J., Trac H., Cen R., Cooray A., 2008, *ApJ*, 689, 1
- Santos M. G., Ferramacho L., Silva M. B., Amblard A., Cooray A., 2010, *MNRAS*, 406, 2421
- Semelin B., Combes F., Baek S., 2007, *A&A*, 474, 365
- Semelin B., Eames E., Bolgar F., Caillat M., 2017, *MNRAS*, 472, 4508
- Shakura N. I., Sunyaev R. A., 1973, *A&A*, 24, 337
- Shapiro P. R., Giroux M. L., Babul A., 1994, *ApJ*, 427, 25
- Shimabukuro H., Semelin B., 2017, *MNRAS*, 468, 3869
- Shimabukuro H., Yoshiura S., Takahashi K., Yokoyama S., Ichiki K., 2016, *MNRAS*, 458, 3003
- Stacy A., Bromm V., Lee A. T., 2016, *MNRAS*, 462, 1307
- Stark D. P., et al., 2015a, *MNRAS*, 450, 1846
- Stark D. P., et al., 2015b, *MNRAS*, 454, 1393
- Stark D. P., et al., 2017, *MNRAS*, 464, 469
- Tamura Y., et al., 2019, *ApJ*, 874, 27
- Tilvi V., et al., 2014, *ApJ*, 794, 5
- Totani T., Kawai N., Kosugi G., Aoki K., Yamada T., Iye M., Ohta K., Hatori T., 2006, in IAU Joint Discussion.
- Ueda Y., Akiyama M., Hasinger G., Miyaji T., Watson M. G., 2014, *ApJ*, 786, 104
- Vieira J. D., et al., 2013, *Nature*, 495, 344
- Villaescusa-Navarro F., Viel M., Datta K. K., Choudhury T. R., 2014, *J. Cosmology Astropart. Phys.*, 9, 050
- Vonlanthen P., Semelin B., Baek S., Revaz Y., 2011, *A&A*, 532, A97
- Watkinson C. A., Pritchard J. R., 2015, *MNRAS*, 454, 1416
- Watkinson C. A., Giri S. K., Ross H. E., Dixon K. L., Iliev I. T., Mellema G., Pritchard J. R., 2019, *MNRAS*, 482, 2653
- Watson D., Christensen L., Knudsen K. K., Richard J., Gallazzi A., Michałowski M. J., 2015, *Nature*, 519, 327
- Wise J. H., Abel T., 2008, *ApJ*, 685, 40
- Woo J.-H., Urry C. M., 2002, *ApJ*, 579, 530
- Xu H., Ahn K., Wise J. H., Norman M. L., O’Shea B. W., 2014, *ApJ*, 791, 110
- Xu H., Wise J. H., Norman M. L., Ahn K., O’Shea B. W., 2016, *ApJ*, 833, 84
- Yajima H., Khochfar S., 2015, *MNRAS*, 448, 654
- Yajima H., Li Y., 2014, *MNRAS*, 445, 3674

APPENDIX A: MULTIPHASE ALGORITHM

Many mesh based calculations adopt the finite-volume approach, which means that the value of a quantity Q inside a cell is the av-

erage of this quantity over the volume of the cell V

$$\langle Q \rangle = \int_V Q dV. \quad (\text{A1})$$

Problems arise when derived quantities rely non-linearly on one or more calculated quantities Q_i , as generally

$$\langle Q^k \rangle \neq \langle Q \rangle^k \quad (\text{A2})$$

if $k \neq 1$. Examples of this in the context of photoionization calculations are the recombinations rates and collisional cooling rates (both are proportional to n^2 , where n is the density). In the context of recombination rates, this discrepancy can sometimes be corrected for by using clumping factors

$$C = \frac{\langle n^2 \rangle}{\langle n \rangle^2}, \quad (\text{A3})$$

if the density variations inside a cell are known.

The width of ionization fronts (I-fronts) is approximately 20 photon mean free paths, which for soft (low-energy) photons is typically much smaller than the spatial resolution in cosmological-volume simulations. Therefore, the I-front transition is quite sharp and cannot be easily resolved. When the radiative transfer code does not resolve ionization fronts, some cells will be partly inside an ionized region, where the hydrogen ionization fraction $x \approx 1$, and partly outside, where $x \approx 0$. Let us assume that a fraction f of a cell is inside and $1 - f$ outside the ionized region. Such a cell can be described as multiphase, as it contains both an ionized phase and a neutral phase. Since for pure hydrogen the recombination rate is proportional to $n(\text{HII})n(e)$ and $n(\text{HII}) = n(e^-) = xn$, the average recombination rate in the cell will be proportional to $f n^2$; whereas, the value derived from the finite volume values of the cell will be $f^2 n^2$, as $\langle n(\text{HII}) \rangle = fn$. This error is usually ignored as it is often transient, around the time the I-front passes through the cell, and relatively small. However, for large cells and weak sources, cells may be in a multiphase state for a long time, and the cumulative error in the recombination calculation may be substantial.

These errors can be much more substantial when calculating the 21-cm signal. The averaged value of the 21-cm signal in a cell is

$$\langle \delta T_b \rangle = \delta \hat{T}_b \left\langle x(\text{HI})(1 + \delta) \left(1 - \frac{T_{\text{CMB}}}{T_s} \right) \right\rangle; \quad (\text{A4})$$

whereas, the finite volume values for the gridded quantities give the estimate

$$\delta T'_b = \delta \hat{T}_b \langle x(\text{HI}) \rangle \langle (1 + \delta) \rangle \left(1 - \frac{T_{\text{CMB}}}{\langle T_s \rangle} \right). \quad (\text{A5})$$

If we assume that $T_s = T$, a fraction f a cell is fully ionized and hot ($T = T^{\text{hot}}$), and the remainder neutral and cold ($T = T^{\text{cold}} < T_{\text{CMB}}$), the average 21-cm signal will be

$$\langle \delta T_b \rangle = \delta \hat{T}_b (1 - f)(1 + \delta) \left(1 - \frac{T_{\text{CMB}}}{T^{\text{cold}}} \right) < 0. \quad (\text{A6})$$

However, the quantity $\delta T'_b$, based on the cell averages, will be

$$\delta T'_b = \delta \hat{T}_b (1 - f)(1 + \delta) \left(1 - \frac{T_{\text{CMB}}}{f T^{\text{hot}} + (1 - f) T^{\text{cold}}} \right) \quad (\text{A7})$$

and positive if $f T^{\text{hot}} + (1 - f) T^{\text{cold}} > T_{\text{CMB}}$, which for $z \sim 15$ and for $T^{\text{hot}} \sim 10^4$ K is true for any $f > 4 \times 10^{-3}$. Clearly, we need to separate the hot and cold states to obtain the correct 21-cm signal.

Such sharp transitions in the ionization fraction and temperature are associated with relatively soft (i.e., low-energy) ionizing photons for which the mean free path is shortest. If the sources can produce both soft and hard (high-energy) ionizing photons, as is the case in the simulations presented in this paper, we need to separate their effects to establish what fraction of a cell is fully ionized by soft ionizing photons and what fraction of the cell is cold and neutral, or is partially ionized by hard photons. In Paper I, we achieved this separation by running two simulations, one with only soft sources and one with both soft and hard sources included. The difference between the two results would then give us the heating and ionization caused by the hard sources alone.

However, while this worked well for the case considered in Paper I, this solution neglects the fact that the code uses the average temperatures and electron fractions to calculate recombination and cooling rates, which are also strongly non-linear functions of the temperature. In addition, it is rather wasteful to run two simulations for every case. We therefore have introduced a different approach in which we let the code internally and self-consistently take into account the multiphase character of the ionization front cells.

This new multiphase code separates and individually tracks the effects of the photoionization and heating rates from the soft and hard sources, Γ^{soft} and Γ^{hard} , and also keeps track of the mass fraction f of a cell that has been ionized by soft sources. Since soft photons have very short mean free paths in neutral or partially ionized media due to their high interaction cross-sections, there is always a sharp boundary outlining the volume affected by them. Cells can be in one of three categories:

(i) Pre-multiphase cells: these cells have never seen a soft ionizing rate above certain minimum value $\Gamma^{\text{soft}} > \Gamma^{\text{soft,lim}}$ and are considered to not be affected by soft ionizing photons. They have a uniform ionization fraction and temperature, determined by Γ^{hard} . These cells produce a 21-cm signal, which is calculated based on the cell-averaged quantities.

(ii) Multiphase cells: these cells have at some point experienced a soft ionization rate $\Gamma^{\text{soft}} > \Gamma^{\text{soft,lim}}$ and a fraction f of these cells affected by soft radiation is assumed to be fully ionized ($x(\text{HI}) = 0$) and heated to T^{soft} . We take $T^{\text{soft}} = 10^4$ K. The value of f depends on the evolution of Γ^{soft} . The ionization and thermal state of the rest of the cell, $1 - f$, is calculated based on the hard-photon rates Γ^{hard} . Only this $1 - f$ cell fraction contains any neutral gas, and thus only it produces a 21-cm signal.

(iii) Post-multiphase cells: these cells have become fully ionized by soft ionizing sources, or in other words $f \approx 1$. In practice, we set a limit of $f^{\text{lim}} = 0.999$ above which we consider a cell to have reached this state. We calculate the ionization fraction and temperature based on the total rates $\Gamma^{\text{soft}} + \Gamma^{\text{hard}}$. These cells do not produce any appreciable 21-cm signal.

The minimal ionization rate needed for cells to become multiphase is set to $\Gamma^{\text{soft,lim}} = 10^{-5}/\Delta t$, where Δt is the time step. This threshold implies that the soft ionizing photons can ionize a fraction $f = 10^{-5}$ of the cell within one time step. We found in tests that for the resolution and time step we use (~ 1 Mpc and ~ 5 Myr), this limit correctly identifies ionization front location cells.

For the multiphase cells, we only calculate the hydrogen ionization fraction, which we equate to the fraction f that has $x(\text{HII}) = 1$. We assume that inside this fraction f of the cell affected by soft photons the helium ionization state [$x(\text{HeI}), x(\text{HeII}), x(\text{HeIII})$] will be $[0, 1 - x(\text{HeIII}), x(\text{HeIII})]$,

where $x(\text{HeIII})$ is set by the hard sources and is assumed to have this value over the entire cell.

Algorithmically, the code first considers the effect of the soft ionizing sources. By ray tracing from these sources and calculating the ionization rates from them, we establish which cells are in which of the above three categories. For the multiphase cells, we find the value of f . Since we assume that HeII follows HII and that the temperature is T^{soft} , we only calculate the hydrogen ionization rates during this step. Because we have multiple soft sources contributing to a cell, we iterate to obtain converged values for f . The recombination rates are calculated assuming the temperature T^{soft} .

After this step, we ray trace again, but now considering both hard and soft sources, calculating the H and He photo-ionization rates as well as the heating rates. For the pre- and post-multiphase cells, we apply the sum of the contributions of all sources. For the multiphase cells, we disregard the contribution of the soft sources, since their contribution to the ionization was accounted for in the first step.

We therefore only apply the rates from the hard sources to the fraction $1 - f$ of the multiphase cells. We once again iterate over all sources to obtain convergence on the ionization fractions and temperatures of the pre- and post-multiphase cells, as well as in the fraction $1 - f$ of the multiphase cells. For the multiphase cells, we use recombination and cooling rates calculated from the temperature of the $1 - f$ fraction of the cells that follows from the heating by hard sources.

APPENDIX B: DESCRIPTION OF TEST SIMULATION RESULTS

In order to test and verify our new method, we have run a series of idealized test cases, as summarized below. First, we briefly recap the original method used to correct our simulations. As described in Paper I, the temperature calculated by the original method is given by:

$$T_{\text{HI},x} = \frac{T_{c,x} - T_{\text{HII},s}x}{1 - x}, \quad (\text{B1})$$

where $T_{c,x}$ is the temperature from the C²-RAY X-ray simulation, x is the ionized fraction, and $T_{\text{HII},s}$ is the temperature of the ionized region given by:

$$T_{\text{HII},s} = \frac{T_{c,s} - T_{\text{ad}}(1 - x)}{x}. \quad (\text{B2})$$

Here, $T_{c,s}$ is the temperature from the stellar-only run, and T_{ad} is the adiabatic temperature of the universe.

B1 Test 1: Comparison to a High-Resolution box

Firstly, we compare the raw outputs of the multiphase and old version of the code both at high (3.25 kpc h^{-1} per cell) and simulation resolution (0.976 Mpc h^{-1} per cell) for a 2.928 Mpc h^{-1} box. Boxes have a single, stellar-only source in the box centre with the average luminosity of a stellar source in our simulations (10^{50} ionizing photons per second), and the test is run from $z = 23.268$ until $z = 22.67$.

In Fig. B1, we show the result from Test 1 for $T_{c,x}$ (top) and δT_b (bottom) cross-sections through the forming HII region. The results from the high-resolution box (thin red line) are correct despite using the original method, since the ionization front has been

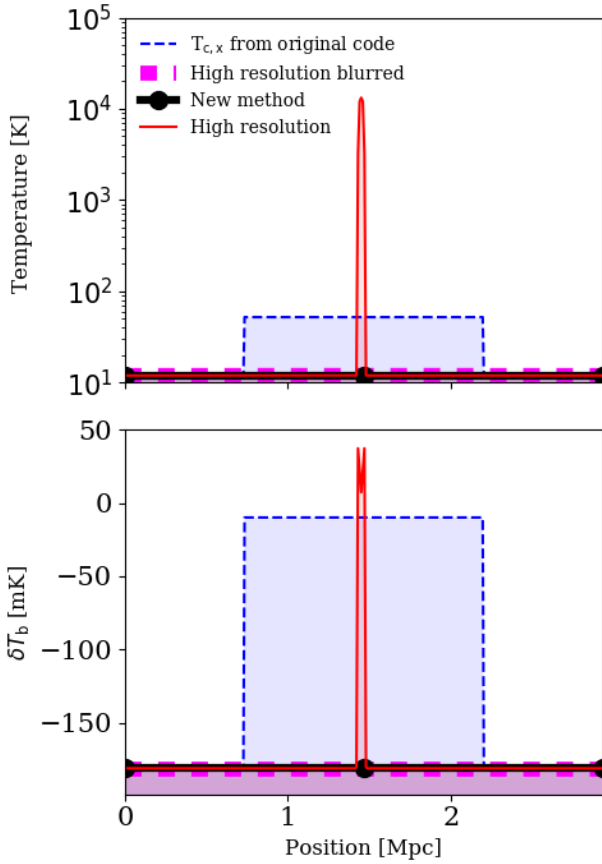


Figure B1. Test 1: Comparison of our new multiphase radiative transfer method to the previous, old C²-RAY code, as well as to a high-resolution simulation using the old method for a typical stellar-only source at $z = 22.67$. The plot shows cross section of the kinetic temperature (top) and δT_b (bottom). The temperature is over estimated in the original method when compared to the high-resolution case. The multiphase method, however, yields the same result as the high-resolution run when it is smoothed to the resolution of the simulation. In the lower panel, we can see that the old method predicts a signal of emission; whereas, the new method and smoothed, high-resolution run give the expected result for a source with no X-rays, i.e. absorption from the cold gas in the surrounding cells.

fairly well resolved. Currently, computational resources are insufficient to run a full simulation box at this resolution; otherwise, high-resolution runs would be a valid solution.

In order to compare the results at the resolution of our large-scale simulations, we coarsen these results to the relevant resolution (thick orange line). As shown in the upper panel, the original method (dashed blue line) clearly overestimates the temperature of the neutral IGM when compared to the smoothed high-resolution run. However, the multiphase method (dotted purple line) is in agreement with the smoothed high-resolution box.

Fig. B1 (lower panel) shows the impact this overestimation of the temperature of the neutral IGM has on δT_b . The old code (blue dashed line) predicts δT_b to be much higher, and partly in emission, than the value calculated from the high-resolution box that is smoothed to simulation resolution (thick orange line). The multiphase method (dotted purple line) again agrees with the smoothed high-resolution box (thick orange line). Note that the high-resolution run does in fact show a small amount of emission

due to photons from the harder end of the blackbody spectrum and (still) insufficient resolution to fully resolve the I-front. However, clearly these heated regions do not contribute significantly to δT_b .

B2 Test 2: Comparison to δT_b calculation method used in Paper I

We compare the new multiphase method to the correction method we used in Paper I by performing two additional constant density test simulations at a resolution twice the critical density of the universe (the effect of varying the density of the boxes was checked and concluded to be minimal). All boxes have luminous sources in the centre with the same parameters as in Table 1: only stars (S1), and in combination with HMXBs (S4), QSOs (S2 and S3), and all types (S5). The luminosity of HMXBs were typical of our simulations (10^{49} ionizing photons per second). QSO sources have a luminosity of 10^{52} ionizing photons per second and do not switch on until $z \sim 20$. As in the simulation, they are active for 34.5 Myr.

The results of these tests are shown in Fig. B2 alongside results from the lower resolution boxes considered in Test 1. As the multiphase and original method treat the cells without stellar radiation equivalently, we focus on the values of the source cell only (in both of these tests the ionized bubble never leaves this cell). In Fig. B2 (left), we show the hydrogen ionized fraction evolution produced by the two methods. The ionized fraction of hydrogen is slightly lower in the original case for all test boxes, which is due to the fact that recombination rates were previously calculated from the average temperature and hydrogen ionized fraction of the cell and therefore were systematically overestimated. In the new method, recombination rates are calculated for ionized hydrogen at the assumed temperature of the ionized region (10^4 K). Apart from this minor difference, both original and multiphase methods display the same smooth evolution.

In Fig. B2 (middle), we show the evolution of the $T_{\text{HI},x}$ of the source cell, comparing the new multiphase method (solid) and the original method (calculated as described in Paper I). We can see that, for all sources, the two methods are in agreement. In the right panel of this figure, we show δT_b for both methods and all source types. Again, the two methods are in excellent agreement.

We therefore conclude that the multiphase method and our previous correction method of calculating δT_b using post-processing can both be used for all sources. However, there are limitations of the original method, which are described in the following section.

B3 Test 3: Limitations of the Original Correction Method

The multiphase and original correction methods diverge from one another when the temperature rises above 10,000 K. As discussed above, the original correction method requires two simulations: one with X-rays and one without. At temperatures greater than 10,000 K, radiative hydrogen-line cooling due to collisional excitations becomes efficient. This cooling effectively caps the gas temperatures given by the two original simulations: $T_{c,s}$ and $T_{c,x}$, and therefore the value for $T_{\text{HI},x}$ (calculated using Equations B2 and B1) is underestimated and becomes unreliable. In addition, as the X-ray simulation yields slightly higher temperatures, cooling occurs more rapidly when sources are switched off. In this case, $T_{c,s}$ can even become larger than $T_{c,x}$, meaning that the original method can even formally yield negative temperatures in some cells.

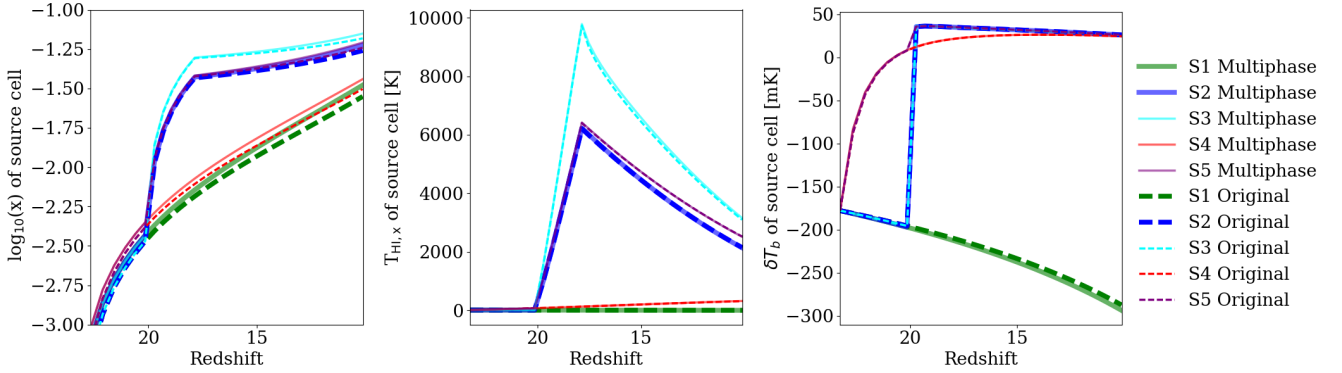


Figure B2. Test results comparing the new multiphase method and the old code. On the left, we show the ionized fraction evolution with the ‘classic’ method (dashed lines) and the new multiphase method (solid lines). In the middle panel, we show the mean temperature evolution using the multiphase method (solid lines), the ‘classic’ method (dotted lines), and the original method after the correction described in Paper I (dashed lines). Finally, on the right, we show δT_b , following the same notation as the middle panel.

We demonstrate this effect using a simulation-resolution test box containing a bright star (1×10^{52} ionizing photons per second) and a QSO (with 1×10^{51} ionizing photons per second) inside. The QSO switches on at $z \sim 20$ and then turns off at $z \sim 18$.

The top panel of Fig. B3 shows the temperature of the source cell. The value of T_{HI} from the new multiphase version of the code is plotted using the solid blue line. This temperature remains low at early times as there is no X-ray heating. When the QSO switches on, T_{HI} from the multiphase version of the code continues to rise until the QSO switches off. After this, T_{HI} cools slowly, remaining well above T_{CMB} .

The values of $T_{c,s}$ (green dotted line) and $T_{c,x}$ (blue dotted lines) from the original code are also shown in the top panel of Fig. B3. Both agree until the QSO becomes active, at which point $T_{c,x}$ rises above $T_{c,s}$ due to X-ray heating, as expected. When the QSO switches off, $T_{c,x}$ is greater than $T_{c,s}$, so the X-ray simulation cools more rapidly than the stellar simulation and $T_{c,x}$ briefly drops below $T_{c,s}$. After this, the star in the cell continues heating and ionizing and drives the $T_{c,s}$ and $T_{c,x}$ back up to 10,000 K.

The value of $T_{\text{HI},x}$ calculated from $T_{c,s}$ and $T_{c,x}$ (as described in Equations B1 and B2) is shown with the dashed blue line. The temperature is in agreement with the value given by the multiphase method as long as there is no X-ray heating. When the QSO switches on, $T_{\text{HI},x}$ briefly increases before leveling. This plateau happens as $T_{c,s}$ and $T_{c,x}$ are capped by collisional cooling, meaning that the X-ray heating is vastly underestimated. When the QSO switches off, $T_{\text{HI},x}$ drops below zero (zero is marked with the black dashed line to illustrate where this occurs). This behavior is clearly unphysical and is due to $T_{c,x}$ dropping below $T_{c,s}$. After this, $T_{\text{HI},x}$ returns to its initial, low value as both $T_{c,s}$ and $T_{c,x}$ are capped at approximately 10,000 K. Hence, X-ray heating is underestimated.

In the lower panel of Fig. B3, δT_b is shown. δT_b in both methods increases before there is X-ray heating due to the expanding ionized region created by the bright star in this case, which gradually decreases the neutral fraction. As described above, the multiphase and original correction method agree until until the QSO switches on at $z \approx 20$. When X-ray heating from the QSO begins, δT_b increases rapidly until temperature saturation is reached (the high- T_S limit is marked on with the black dot-dash line). As the T_{HI} from the multiphase method remains above T_{CMB} for the rest of the simulation, δT_b follows the high- T_S limit and slowly decreases towards zero as the ionized region from the star continues

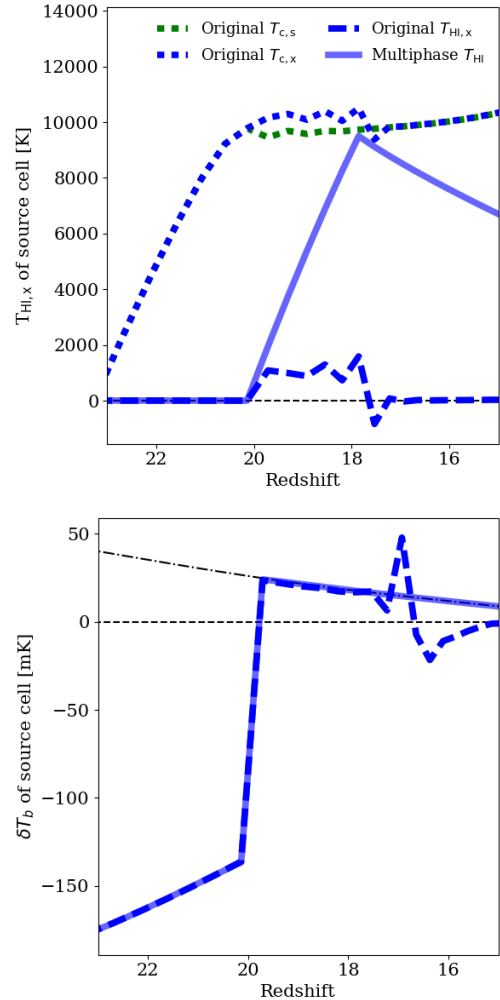


Figure B3. Test runs showing the limitations of the old method. Shown are the evolution of the kinetic temperature, T_K (top), and of the differential brightness temperature, δT_b (bottom), for all test simulations, as labeled. The high- T_S limit is also shown (black dot-dash line).

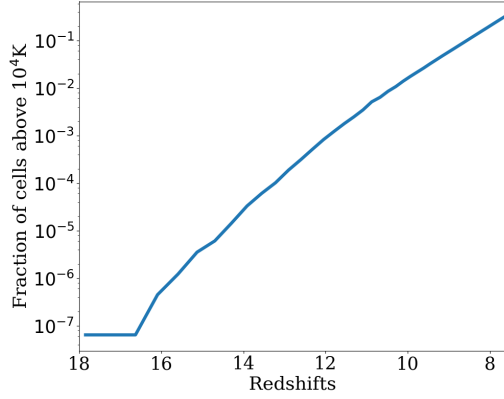


Figure B4. Shown are the fraction of cells that exceed 10,000 K in the stellar-only simulation for the original code. Before $z \approx 18$ there are no cells above 10,000 K. The number remains small before $z \approx 11$ showing that the original corrections method can be used on cells with HMXBs which reach temperature saturation at $z > 12$.

to grow. δT_b from the original corrections method agrees with the multiphase value until the QSO switches off. At this point, $T_{\text{HI},x}$ drops rapidly and becomes unphysical, which causes erratic behavior in the δT_b values obtained using the original method.

This effect does not impact simulations including HMXBs, since in these simulations temperature saturation is reached at $z \sim 12$, which is before any non-negligible number of cells are heated above 10,000 K (see Fig. B4). We confirmed that the results from S4 and S5 (run with the original method) are the same as those given by the multiphase method by running parts of the simulation with both code versions.